Dual Geostationary Lightning Mapper Observations

SCOTT D. RUDLOSKY[a,b] AND KATRINA S. VIRTS[c]

[a] *National Oceanic and Atmospheric Administration, National Environmental Satellite, Data, and Information Service, Center for Satellite Applications and Research, College Park, Maryland*
[b] *University of Maryland, Earth System Science Interdisciplinary Center, Cooperative Institute for Satellite Earth System Studies, College Park, Maryland*
[c] *University of Alabama in Huntsville, Huntsville, Alabama*

(Manuscript received 23 July 2020, in final form 4 January 2021)

ABSTRACT: Two Geostationary Lightning Mappers (GLMs) now observe spatial and temporal lightning distributions over a vast region. The *GOES-16* GLM covers most land areas in the Western Hemisphere, and detects ~4 times as much lightning as the *GOES-17* GLM. Although the continents dominate the lightning distributions year-round, each season exhibits widespread lightning over parts of the Atlantic Ocean and within three broad regions over the Pacific. These oceanic regions demonstrate the key role convective organization plays in producing larger, longer-lasting, and more energetic flashes observed by both GLMs over the oceans. Texture within the flash densities reveals a close relationship with the underlying topography, underscored by the complex diurnal cycles observed along coastlines and in mountainous regions. GLM information beyond flash frequency provides additional insights into storm mode and evolution. For example, over the Sierra Madre Occidental, time series reveal initially small, short-duration GLM flashes growing larger and longer as storms grow upscale. These mesoscale convective systems often transition offshore, contributing to an average flash area maximum over the eastern Pacific. Data quality improves during the study period with tuning of the ground system software. GLM artifacts due to solar intrusion and sun glint greatly diminish following the blooming filter installation, and the second-level threshold filter reduces false events along particular subarray boundaries (i.e., bar artifacts). Analysis of the overlap region reveals a pronounced north–south line near 103°W, with the *GOES-16* (*GOES-17*) GLM detecting more flashes to the east (west) of this line.

KEYWORDS: Atmospheric electricity; Convective storms; Mesoscale processes; Diurnal effects; Seasonal variability; Lightning

1. Introduction

Two Geostationary Lightning Mappers (GLMs) provide continuous real-time lightning monitoring throughout most of the Western Hemisphere. Each GLM captured nearly 24 billion full-disk images during our 548-day study period. The first Geostationary Operational Environmental Satellite (GOES) R-series satellite (*GOES-16*, herafter *G16*) was launched on 19 November 2016 and moved to its operational GOES-East position (75.2°W) on 18 December 2017. The second satellite in the GOES-R series (*GOES-17*, hereafter *G17*) was launched on 1 March 2018. Following a 6-month checkout at 89.5°W, *G17* moved to 137.2°W in November 2018 before becoming GOES-West on 12 February 2019. The *G16* (*G17*) GLM attained provisional performance maturity on 20 December 2019 (19 January 2020), broadening access to these data. Leveraging this 11-month head start, most early GLM research has focused on the *G16* GLM. The *G17* GLM field of view (FOV) is more sparsely covered by ground-based lightning detection networks, so its distributions are of particular interest. This study examines observations from both instruments during the first 18 months of coincident coverage (1 December 2018–31 May 2020).

Rudlosky et al. (2019) described the first 9 months of *G16* GLM observations that included 237 100 495 lightning flashes. The initial GLM results confirmed similar spatial lightning patterns found over longer time periods by many previous studies. For example, 83% (17%) of the GLM flashes occurred over land (ocean). Their study also revealed that the predecessor low-Earth orbiting Lightning Imaging Sensor (LIS) could require up to 35 years to sample the diurnal cycle at a location of interest for the equivalent of the 257 days (~9 months) they studied. The present manuscript considers ~4 times more data to build upon these initial baseline values and document important new GLM insights into total lightning occurrence and variability across the combined *G16* and *G17* domains.

Only four years since becoming reality, the GLM is establishing a legacy of applications likely to become ubiquitous across a wide variety of meteorological domains (Rudlosky et al. 2020). Operational users have eagerly embraced this new source of lightning information and incorporated it into their workflow. A recent GLM value assessment documented societal and economic benefits realized through GLM data use (Rudlosky et al. 2020). The GLM was shown to improve lightning safety, severe thunderstorm and tornado warnings, safety and effectiveness of wildfire response, short-term model forecasts (via data assimilation), precipitation estimation, tropical cyclone diagnosis and warning, and climate applications. The study also described the value GLM yields through filling data gaps and mitigating aviation hazards. The GLM now provides a national and international baseline of publicly available lightning data and establishes a baseline for widespread government and industry implementation.

Corresponding author: Scott D. Rudlosky, scott.rudlosky@noaa.gov

DOI: 10.1175/MWR-D-20-0242.1

Broadening GLM use motivates our documentation of the GLM distributions. Goss (2020) illustrates GLM data helping NWS forecasters make earlier and more confident tornado warning decisions, and describes the importance of observing continuing current lightning flashes. Specifically, the GLM identifies continuing current flashes that are more likely to ignite wildfires (Bitzer 2017; Fairman and Bitzer 2020, manuscript submitted to *J. Geophys. Res.*). Pavolonis et al. (2020), Cecil et al. (2020), and Schultz et al. (2020) revealed that the GLM can aid the detection of volcanic eruptions and characterization of their plumes. The GLM also observes large meteors that explode in the atmosphere (i.e., bolides; Jenniskens et al. 2018). Fierro et al. (2018) suggested that continuous satellite-based total lightning is a promising new tool for studying tropical cyclones. Recent GLM data assimilation (DA) results also are encouraging. Fierro et al. (2019) and Hu et al. (2020) demonstrated improved short-term forecasts of accumulated rainfall, composite radar reflectivity, and individual storm tracks by assimilating GLM data. Kong et al. (2020) found that GLM DA improved representation of both the location of storm cores and the storm extent. Many of these applications employ gridded GLM imagery products (Bruning et al. 2019) derived from the Level 2 (L2) GLM data evaluated herein.

This study documents insights provided by the GLMs' broad spatial and fine temporal coverage as context for researchers and operational users. Section 2 defines the instrument, data, and analysis methods. Section 3 describes the overall annual distributions along with insights gained through examining observations in the region of overlapping coverage. Seasonal distributions illustrate both natural variability and evolving instrument performance. Diurnal variability highlights the usefulness of continuous GLM observations throughout the combined FOV. As the number and variety of operational GLM users continue to grow, so does the importance of documenting and communicating differences between the two GLMs. We characterize the spatial and temporal distributions observed by both GLMs to provide context for applying these data.

2. Data and methods

a. Instrument

The GLM requires optimization of the entire signal chain, from telescope optics to ground processing algorithms, as described by Edgington et al. (2019). Their study detailed the complex technology allowing the GLMs to map lightning flashes over vast regions within seconds of occurrence. The high-volume digital video data (12.5 Gbps) requires onboard processing by a Real Time Event Processor (RTEP) that thresholds each camera frame against a running background average. Reporting of threshold exceedance events on an exception basis reduces downlink bandwidth by three orders of magnitude.

Rudlosky et al. (2019) summarized the GOES-R Product Definition and Users' Guide (PUG; GOES-R Algorithm Working Group 2017) and GOES-R Data Book (NASA 2018) to detail the GLM instrument design and specifications, including the functional characteristics, content, and format of the GLM data. The GLM focal plane is divided into 56 subarrays for fast transient event processing. Each subarray is independently tuned to optimize the dynamic range and sensitivity. The GLM relies on the spacecraft position and pointing information along with a coastline identification and navigation procedure to convert the focal plane x, y to latitude and longitude coordinates. The GLM L2 product navigates observations to an estimated cloud top using an assumed lightning ellipsoid height that varies from 6 km at the poles to 14 km at the equator.

b. Data

The GLM L2 files contain information on GLM events, groups, and flashes (Edgington et al. 2019; Rudlosky et al. 2019; Mach 2020). The GLM observes 503 frames per second to detect sudden changes in brightness relative to a continuously updating background average (Edgington et al. 2019). Event detections trigger when the new samples exceed selectable detection thresholds. Filters in the ground-processing software remove nonlightning events leaving only the 2-ms events most likely to be lightning (Edgington et al. 2019). The Lightning Cluster Filter Algorithm (LCFA) then combines events into groups and groups into flashes (Mach 2020). GLM groups represent one or more simultaneous GLM events observed in adjacent pixels, and GLM flashes include one or more sequential groups separated by less than 330 ms and 16.5 km (Mach et al. 2007).

Assumptions in the LCFA are required to meet latency requirements, motivating examination by two recent studies. The operational algorithm limits the events per group and groups per flash to 101, and the flash duration to 3 s to keep up with real-time processing (Mach 2020). The computational limits imposed on the GLM clustering algorithm only affect the group and flash results when local flash rates exceed ~40 per minute (Mach 2020). Peterson (2019) evaluated the operational LCFA performance, identified ground system processing anomalies, and mitigated flash cluster degradation. His study found that the operational LCFA artificially splits a small fraction of GLM flashes (<4%), and produced a reclustered flash dataset that emphasizes cluster integrity over data latency and computational expense. As expected, the postprocessed values all exceeded those reported by Rudlosky et al. (2019), with the average flash covering 501 km^2 over 321 ms (versus 454 km^2 and 301 ms). The splitting effect is most noticeable at the extremes, with one especially complex flash artificially split into 33 flash clusters. While important to consider, these clustering anomalies only impact the completeness not the validity of the operational L2 data (Peterson 2019). Future analyses will more closely examine the influence of flash splitting on the observed GLM patterns. The present study reports on the L2 data without additional post processing.

Studies using ground-based reference networks have found that the *G16* GLM meets design specifications of >70% detection efficiency (DE) and <5% false alarm rate (FAR) when averaged across 24 h, despite known limitations and artifacts. Bateman and Mach (2020) evaluated the *G16* GLM performance using reference data from the World Wide Lightning

Location Network (WWLLN; Rodger et al. 2004), Earth Networks Total Lightning Network (ENTLN; Lapierre et al. 2019), and Vaisala's Global Lightning Dataset (GLD360; Murphy and Said 2020) and National Lightning Detection Network (NLDN; Cummins and Murphy 2009). They showed an overall detection efficiency (DE) of 77%, with values throughout most of the FOV exceeding the design specification of 70% over 24 h. Their day/night plots revealed that the GLM performed well during day (73%) and improved at night (82%). The false alarm rate (FAR) analysis is complicated by spatially varying DE within each of the reference datasets, with the 5% FAR specification left unmet for much of the GLM FOV. Bateman and Mach (2020) found the best GLM performance in regions with the best quality ground truth data, suggesting that the GLM failure to meet the FAR specification may be due to the lack of corroborating "ground truth" data. The GLM data quality continually improves as calibration and validation efforts identify issues and implement patches in the ground system software.

Although the GLM meets DE design specifications, studies have shown variability that must be understood to confidently apply the GLM observations. Murphy and Said (2020) showed that the *G16* GLM DE begins to drop off within about 2000 km of the FOV edge, particularly over land. They also noted low GLM DE associated with some severe storms with very high midaltitude reflectivity, consistent with the idea that large multiple scattering pathlengths, together with absorption of the near-infrared signals by water (in all of its phases), depresses the GLM DE. They noted additional factors that might contribute to this low DE, including time of day, flash energetics, and the incident angle at the GLM sensor. Rutledge et al. (2020) showed particularly low GLM DE for electrically "anomalous" storms in Colorado, and associated this observation with intense cloud water and cloud ice contents and compact flashes at mid- to low levels in these storms. Zhang and Cummins (2020) evaluated the GLM DE in central Florida using the Kennedy Space Center Lightning Mapping Array (KSC LMA). The mean daily flash DE was 73.8% with the best detection at night. The GLM reported 86.5% of LMA flashes with coincident cloud-to-ground return strokes reported by the U.S. National Lightning Detection Network. Their results revealed flash size and duration to be key parameters influencing GLM DE. Regardless of storm type, they found 20%–40% DE for small (5–8-km channel length) and short-duration (<0.3 s) flashes, and greater than 95% DE for large (50–100-km channel length) and long-duration (>0.5 s) flashes.

Efforts continue toward fine tuning the GLMs through onboard adjustments and ground processing algorithm modifications. Rudlosky et al. (2019) and Bateman and Mach (2020) described the influence of instrument observing artifacts on the resulting distributions. Table 1 lists noteworthy updates to the ground system software during the study period. Most updates seek to remove or reduce artifacts related to sun glint, solar intrusion during eclipse season, inconsistencies at subarray boundaries, or disturbances to platform stability. The second-level threshold filter was applied on 27 February 2019 to mitigate the bar artifacts described by Rudlosky et al. (2019). The issue worsened until an update on 30 April 2019 that better tuned the filter and mitigated the bar artifacts. An even greater impact accompanied the blooming filter, implemented on 25 July 2019 to quench the rapid growth of sun-glint and solar intrusion artifacts. This filter also decreases the need for an overflow valve that temporarily halts processing and can result in a series of empty 20-s files (recognizable by L2 files with ~80 kb sizes). Following this update, the GLM L2 product also correctly indicates yaw flip state (i.e., satellite orientation relative to the axis pointed toward the center of Earth; previously used a fill value).

TABLE 1. GLM-related updates to the GOES ground system software during the study period.

Update	Date	Update description
PR.07.08.00	27 Feb 2019	1) Second-level filter code change 2) Data burst filter code change
PR.07.10.05	30 Apr 2019	1) Threshold changes to mitigate noise 2) Turn on contrast leakage filter 3) Update second-level threshold to better handle bar artifacts
DO.08.00.00	25 Jul 2019	1) Implemented blooming filter 2) GLM L2 product outputs correct yaw flip state 3) Minor corrections to the GLM event navigation
PR.08.03.04	2 Oct 2019	1) Updated event energy scale factor and offset

While the *G16* GLM FOV remains static throughout the year, the *G17* GLM has two slightly different fields of view depending on the season (Fig. 1). A cooling issue with the *G17* Advanced Baseline Imager (ABI) requires biannual yaw flips to mitigate thermal channel noise (Sullivan 2020). During our study period, *G17* yaw flips occurred on 27 March 2019, 9 September 2019, and 6 April 2020. Yaw flips revealed nonuniformity along the edges of the GLM detector array. For the *G17* GLM, the solid (dashed) line in Fig. 1 depicts coverage during boreal summer (winter).

c. Methods

This study examines both the *G16* and *G17* GLM during the first 18 months of coincident coverage (1 December 2018–31 May 2020). The data are characterized as originally produced and archived, except for quality control steps that help mitigate known false events. Each GLM L2 data file includes a flash_quality_flag and a group_quality_flag for which integers > 0 indicate degraded flashes or groups. This study removes flashes with flash_quality_flag $\neq 0$ and groups with group_quality_flag $\neq 0$. Groups also are removed if the parent flash has flash_quality_flag $\neq 0$, and events are removed if the parent group (grandparent flash) has group_quality_flag $\neq 0$ (flash_quality_flag $\neq 0$). The GLM L2 dataset omits both single event and single group flashes to mitigate noise associated with radiation incident on the instrument focal plane.

Spatial maps at 0.1° resolution (~10×10 km^2) complement summary statistics and time series plots to describe seasonal,

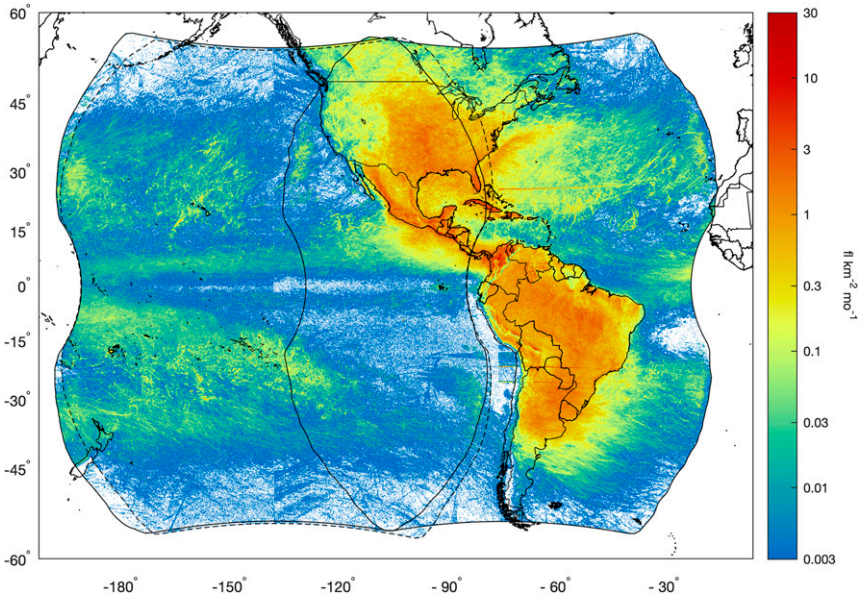

FIG. 1. Combined *G16* and *G17* flash densities during 1 Dec 2018–31 May 2020 with units of flash count per square kilometer per month. Flashes observed by either sensor are included in the overlapping region. Black lines indicate the nominal field of view boundaries for both instruments. For *G17*, the solid (dashed) line depicts coverage during boreal summer (winter).

regional, and diurnal variability. This study illustrates GLM flash density, area, duration, and energy, and quantifies additional flash- and group-level metrics. Flash and group properties are accumulated using their centroid locations (i.e., no consideration of the event footprints/spatial extent of groups and flashes). Tables provide mean, median, 90th, and 99th percentile values for each GLM quantity. For computational efficiency, daily percentile values are calculated, with the table reporting medians of the daily 50th, 90th, and 99th percentile values. Daily standard deviation values are averaged for use in significance testing of mean comparisons.

The large overlap region between the two instruments and the varied *G17* GLM FOV due to yaw flips complicate methods for plotting combined GLM annual distributions. To ensure each calendar month receives equal weight (despite including two DJF/MAM and one JJA/SON), the annual map reports an average of 12 monthly distributions. The monthly distributions consider the number of days each pixel was within the nominal FOV. To prevent double-counting of flashes in the overlap region, we first ran a matching algorithm on *G16/G17* flashes with matching windows of 200 ms and 50 km between flash centroids (matching criteria were selected following sensitivity tests, not shown). Flashes in the overlap region include all *G16* flashes plus the *G17* flashes not observed by *G16*. Hourly and diurnal plots also ensure that each calendar month receives equal weight.

3. Results and discussion

a. Annual distributions

The combined *G16*/*G17* GLMs provide lightning detection over a vast region stretching from an arc connecting the Aleutian Islands and New Zealand eastward to the western coast of Africa (Fig. 1). Spatial flash density patterns closely resemble those shown by previous studies using various lightning datasets (e.g., Boccippio et al. 2000; Christian et al. 2003; Ortéga and Guignes 2007; Nesbitt et al. 2008; Pessi and Businger 2009; Albrecht et al. 2011; Virts et al. 2013; Cecil et al. 2014; Virts et al. 2015; Albrecht et al. 2016; Rudlosky et al. 2019). Flash density values exceeding 1 flash km^{-2} $month^{-1}$ occur almost exclusively over land, with relative maxima and minima related to well-known meteorological and topographic influences. The lightning maximum for the combined GLM domain occurs in Venezuela and Colombia where some locations experience more than 10 flashes km^{-2} $month^{-1}$ (maxima also found by Albrecht et al. 2016). Relative maxima with >3 flashes km^{-2} $month^{-1}$ appear over Florida, the Sierra Madre Occidental in Mexico, and Cuba.

Texture within the flash densities reveals the close relationship between lightning occurrence and the underlying topography. The sharpest flash density contrasts coincide with coastlines and mountain ranges, with clear examples occurring throughout the tropics and along the western coast of South America. Above the Andes Mountains, from Bolívar Peak in Venezuela (8.5°N, 71.1°W) to La Paz, Bolivia (16.5°S, 68.1°W), relative minima along the highest peaks occur very near relative maxima along their foothills. A lack of lightning along the immediate Pacific coast of South America reveals the year-round calming influence of the southeast Pacific anticyclone (Muñoz and Garreaud 2005; Garreaud and Muñoz 2005; Barrett and Hameed 2017). More subtle variations in the Amazon rain forest indicate the influence of rivers and river breeze fronts on lightning occurrence (Albrecht et al. 2011; dos Santos et al. 2014; Burleyson et al. 2016; Machado et al. 2018).

Peterson (2019) further details GLM observations in South America.

Lightning occurs much less frequently offshore (Fig. 1) where relative maxima coincide with islands, warm sea surface temperatures, large-scale convergence zones, and midlatitude storm tracks. Relative maxima surrounding the Caribbean and Polynesian islands relate to contrasting surface heating between land and sea (Williams et al. 2004) and more diverse atmospheric composition (i.e., differences in the concentrations of cloud condensation nuclei) relative to conditions over the open ocean (Williams et al. 2002). The relative maxima associated with the Pacific intertropical convergence zone (ITCZ) exhibits interesting seasonal and diurnal variability further detailed in sections 3b and 3c, respectively. Subtle features should become more pronounced with more data, and future studies are encouraged to link these patterns to physical processes (e.g., examining the role of shipping lanes in the offshore distributions, Thornton et al. 2017).

The influence of the Gulf Stream Current appears as a pronounced region of enhanced flash densities east of North America (exceeding 1 flash km^{-2} $month^{-1}$). Virts et al. (2015) showed a broad diurnal lightning frequency maximum over the Gulf Stream from evening through noon the following day, and related this maximum to winds blowing off the continent and converging above the Gulf Stream. During winter, lightning exhibits a weak diurnal cycle over the Gulf Stream, with lightning most frequent during the evening (Virts et al. 2015). This is indicative of midlatitude storm systems that often weaken immediately offshore only to reinvigorate when encountering the more favorable maritime environment above the Gulf Stream. Relative maxima downwind of both continents (Fig. 1) suggest that the mesoscale convective systems (MCS) responsible for much of the lightning over North and South America continue producing lightning as they transition offshore (see discussion of seasonal cycles over the Atlantic Ocean in section 3b).

The *G16* GLM covers most land areas in the Western Hemisphere, and thus observes ~4 times as much lightning as the *G17* GLM. During our study period, the *G16* (*G17*) GLM observed 480 (130) million flashes, 7.5 (1.8) billion groups, and 19.4 (4.4) billion events. The average *G16* (*G17*) GLM flash consists of 15.6 (14.0) groups and 40.9 (33.6) events, covering 447.2 (423.9) km^2 over a duration of 297.0 (286.1) ms, while producing 249.6 (395.5) fJ of optical energy at instrument aperture (Table 2). The 99th percentile *G16* (*G17*) GLM flashes covered 2590 (2610) km^2 over 1140 (1140) ms. Recall that occasional flash splitting reduces the average group and event counts, area, and duration per flash. However, since the LCFA only degrades flashes when they exceed 100 groups or 3-s duration, noteworthy differences between the L2 and reprocessed statistics only appear at the extremes (e.g., 99.9th percentile values from Peterson 2019; 5966 km^2 area and 3764-ms duration). The much larger average flash energy for *G17* is expected given the different FOVs (i.e., more ocean in *G17* FOV, see next paragraph). Although observing more oceanic regions also suggests larger and longer-lasting average *G17* GLM flashes, they are marginally smaller and shorter duration than the average *G16* flashes. The *G16* GLM observes both the North and South American hotspots for GLM megaflashes reported by Peterson (2021, their Fig. 1a), while the *G17* GLM only observes North American megaflashes, likely contributing to the slightly larger, longer-duration average *G16* flashes.

TABLE 2. Mean, median, 90th, and 99th percentile values of *G16* GLM and *G17* GLM flash and group characteristics during 1 Dec 2018–31 May 2020.

	Mean	50th	90th	99th
G16 GLM				
Flash area (km^2)	447.2	288.8	941.0	2590
Flash duration (ms)	297.0	236.5	620.0	1140
Flash energy (fJ)	249.6	84.28	632.0	2350
Groups per flash	15.6	9.0	38.0	81
Events per flash	40.9	21.0	103.0	263
Events per group	2.6	2.0	5.0	15
Group area (km^2)	181.1	135.5	352.0	1020
Group energy (fJ)	16.0	6.1	33.6	151
G17 GLM				
Flash area (km^2)	423.9	290.1	974	2610
Flash duration (ms)	286.1	220.9	605	1140
Flash energy (fJ)	395.5	146.5	1080	4090
Groups per flash	14	9	39	82
Events per flash	33.6	17	100	278
Events per group	2.4	2	5	13
Group area (km^2)	185.2	139.5	366	1020
Group energy (fJ)	28.6	10.7	56.5	275

Table 3 documents land–sea lightning contrasts. The *G16* (*G17*) FOV includes ~29% (~12%) land, over which 85% (66%) of observed flashes occur. Studies using both ground- and space-based lightning observing networks have shown that although less frequent (Albrecht et al. 2016; Cecil et al. 2014; Christian et al. 2003), lightning flashes over the ocean are stronger, brighter, and longer duration than flashes over land (Boccippio et al. 2000; Mach et al. 2010; Hutchins et al. 2012; Said et al. 2013; Nag and Cummins 2017; Peterson et al. 2017; Bang and Zipser 2019). Both the *G16* and *G17* GLMs report larger (535.4, 551.7 km^2), longer-lasting (336.5, 318.7 ms), and more energetic (410.7, 529.0 fJ) flashes over ocean than land (431.3, 357.8 km^2; 289.9, 269.9 ms; 220.7, 326.4 fJ; Table 3). These mean comparisons are all significant at the $P < 0.0001$ level (not shown). Bang and Zipser (2019) summarize research contrasting lightning over land and oceans, then document the key role convective organization plays in the development of the larger, longer life cycle oceanic storms that produce lightning. Anvil and stratiform clouds often contain horizontally large and layered charge structures that are conducive to lateral flash development (e.g., Weiss et al. 2012; Bruning and MacGorman 2013; Wang et al. 2018), making them favored regions for optically extreme (brightness and duration) lightning flashes (Peterson 2019, 2021). Highly radiant "superbolts" occur in two scenarios: embedded within raining stratiform regions or in nonraining boundary/anvil clouds where optical emissions can take a relatively clear path to the satellite (Peterson et al. 2020). These observations combine to suggest that the tendency for oceanic lightning to occur within larger,

TABLE 3. *G16* GLM and *G17* GLM mean flash and group characteristics over all land and ocean, only over land, only over ocean, and the percent difference between land and ocean during 1 Dec 2018–31 May 2020.

	All	Land	Ocean	Difference (%)
G16 GLM				
Flash count	4.804×10^8	4.073×10^8	7.309×10^7	−69.6
Flash area (km^2)	447.2	431.3	535.4	23.3
Flash duration (ms)	297.0	289.9	336.5	15.7
Flash energy (fJ)	249.6	220.7	410.7	76.1
Groups per flash	15.6	14.7	20.5	37.1
Events per flash	40.9	38.5	54.8	39.8
Events per group	2.6	2.6	2.7	5.1
Group area (km^2)	181.1	178.5	191.7	7.3
Group energy (fJ)	16.0	15.0	20.1	31.7
G17 GLM				
Flash count	1.307×10^8	8.614×10^7	4.453×10^7	−31.8
Flash area (km^2)	423.9	357.8	551.7	45.7
Flash duration (ms)	286.1	269.2	318.7	17.3
Flash energy (fJ)	395.5	326.4	529.0	51.2
Groups per flash	14.0	11.3	19.2	56.3
Events per flash	33.6	25.4	49.5	71.8
Events per group	2.4	2.2	2.6	19.1
Group area (km^2)	185.2	170.5	201.9	17.0
Group energy (fJ)	28.6	29.0	28.3	−2.5

longer-duration, and more organized storm systems contribute to the larger, longer-lasting, and more energetic flashes observed over oceans by both sensors.

Overlapping observations reveal similarities and differences between the *G16* and *G17* GLM observations (Figs. 2 and 3). The overall spatial flash density patterns generally agree between the *G17* (Fig. 2a) and *G16* (Fig. 2b) GLMs, although the *G17* GLM distributions appear noisier (e.g., the south-central Pacific Ocean, Figs. 2a,d). The most prominent feature in Fig. 2 is a north–south line near the center of the overlap region (~103°W), east (west) of which the *G16* (*G17*) GLM detects more flashes (Fig. 2c). Light blue shades indicate that the *G17* GLM observes 20%–40% fewer flashes east of this line, and red shades indicate the *G16* GLM observes 50%–90% fewer flashes over the northwest United States. In the northwest United States, the *G16* GLM only observes 25%–45% of the *G17* GLM observed flashes (Fig. 2d). These observations reveal the influence of varying pixel size and viewing geometry on flash density distributions. Reduced *G16* GLM performance in the northwest United States relates to the proximity to the edge of the FOV, where larger pixels and steeper viewing angles reduce the instrument sensitivity. This limitation also appears for the *G17* GLM, with similarly poor relative performance over the eastern United States near the edge of its FOV.

The *G17* and *G16* GLM distributions of average flash area (Figs. 3a–c), energy (Figs. 3d–f), and duration (Figs. 3g–i) document important natural variability and instrument observing artifacts. The sharpest contrasts appear between land and ocean. Recall that on average GLM flashes are larger, longer duration, and more energetic over oceans than land (Table 3). Average flash area shows the sharpest land/ocean contrast (Figs. 3a,b), particularly near Central America, where mean flash areas over the near-coastal Caribbean and eastern Pacific are nearly a factor of 3 larger than those above the adjacent land. Both sensors observe an east–west contrast in the United States, with smaller (larger) average flashes to the west (east). Average flash duration also exhibits this east–west contrast with shorter (longer) average duration to the west (east), although the signature is less pronounced for the *G17* GLM. Both sensors report weaker flash energies in the U.S. Great Plains and much of Mexico. Instrument detection variability still conceals some natural variability, so continued improvements to GLM ground processing software coupled with increasing data volume will continue providing important and impactful insights.

The overlap region provides an opportunity to describe instrument performance specifics that are less evident when viewing data from individual sensors. Sun-glint and solar intrusion artifacts do not occur in the same places or times for the two instruments, so these artifacts appear as blue shades in Figs. 2d and 2e. Sun-glint artifacts include anomalously small (blue), long-duration (red) flashes (Fig. 3). The clearest sun-glint examples occur in the southeast portion of the overlap region for *G17* (Figs. 3a,g) and the northwest portion for *G16* (Figs. 3b,h). Future studies will encounter much less pronounced solar artifacts with the blooming filter now in place (see section 3b). As expected, average flash energies are larger near the edge of the FOV for each sensor (Figs. 3d,e). Near the FOV edge, larger GLM pixels require more light to trigger, reducing the number of weak GLM events and increasing the average flash energy. Somewhat counterintuitively, larger pixels also result in smaller average flash areas (Figs. 3a–c). Dim events that remain below threshold in larger pixels often occur along the edges of flashes, and fewer edge pixels exceeding threshold reduces the average flash size. Figures 3d–f reveal stripes in the energy distributions that result from the first rows along the leading edges of subarray boundaries being

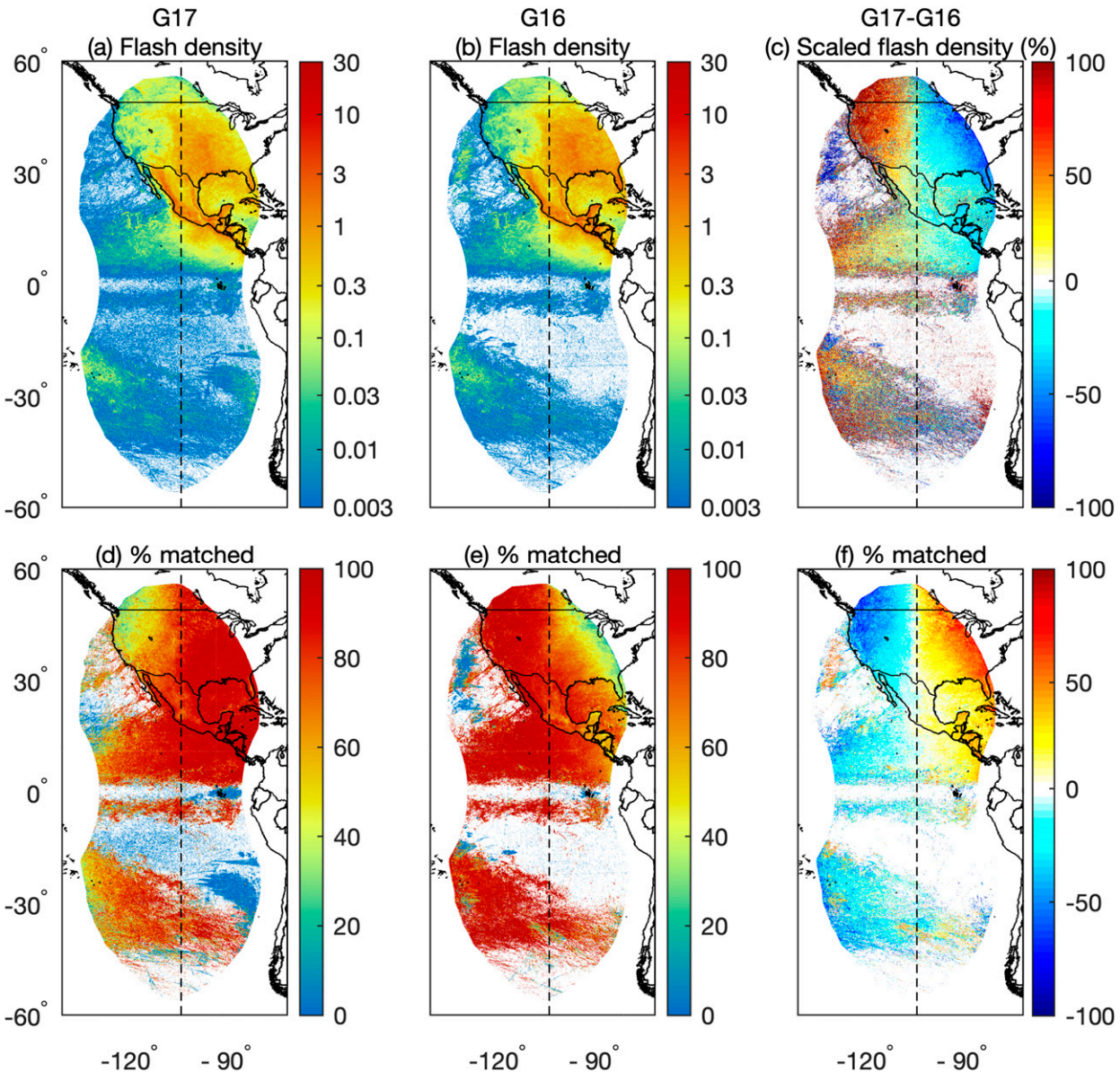

FIG. 2. Region of overlapping coverage between the *G17* and *G16* GLMs: (a) *G17* flash density, (b) *G16* flash density, (c) *G17* minus *G16* flash densities scaled to percentage for emphasis, (d) percentage of *G17* flashes observed by *G16*, (e) percentage of *G16* flashes observed by *G17*, and (f) *G17* minus *G16* percentage matched.

more sensitive (termed overshoot). Prior to the second level threshold filter, RTEP thresholds were set for the entire subarray, permitting weaker events in the first rows. The second level threshold filter reduces but does not completely eliminate this overshoot effect.

b. *Seasonal distributions*

The seasonal *G16* and *G17* GLM flash density distributions illustrate both natural variability and evolving instrument performance (Figs. 4 and 5). Panels each characterize individual 3-month periods, with two DJF and MAM periods that show improving data quality. Both the annual (Fig. 1) and seasonal (Figs. 4 and 5) flash density plots have units of flash count per square kilometer per month, so some local values in the seasonal plots exceed collocated values in the annual plot. The GLM-observed seasonal variability matches patterns shown by other studies (e.g., Virts et al. 2013; Cecil et al. 2014; Albrecht et al. 2016), with most differences related to GLM-specific artifacts. This section first describes differences related to GLM-specific artifacts then documents the GLM-observed seasonal variability.

Seasonal plots reveal diminishing GLM artifacts and improving data quality. Noisier patterns during DJF 2018/19 (Fig. 4a) and MAM 2019 (Fig. 4b) contrast with a cleaner

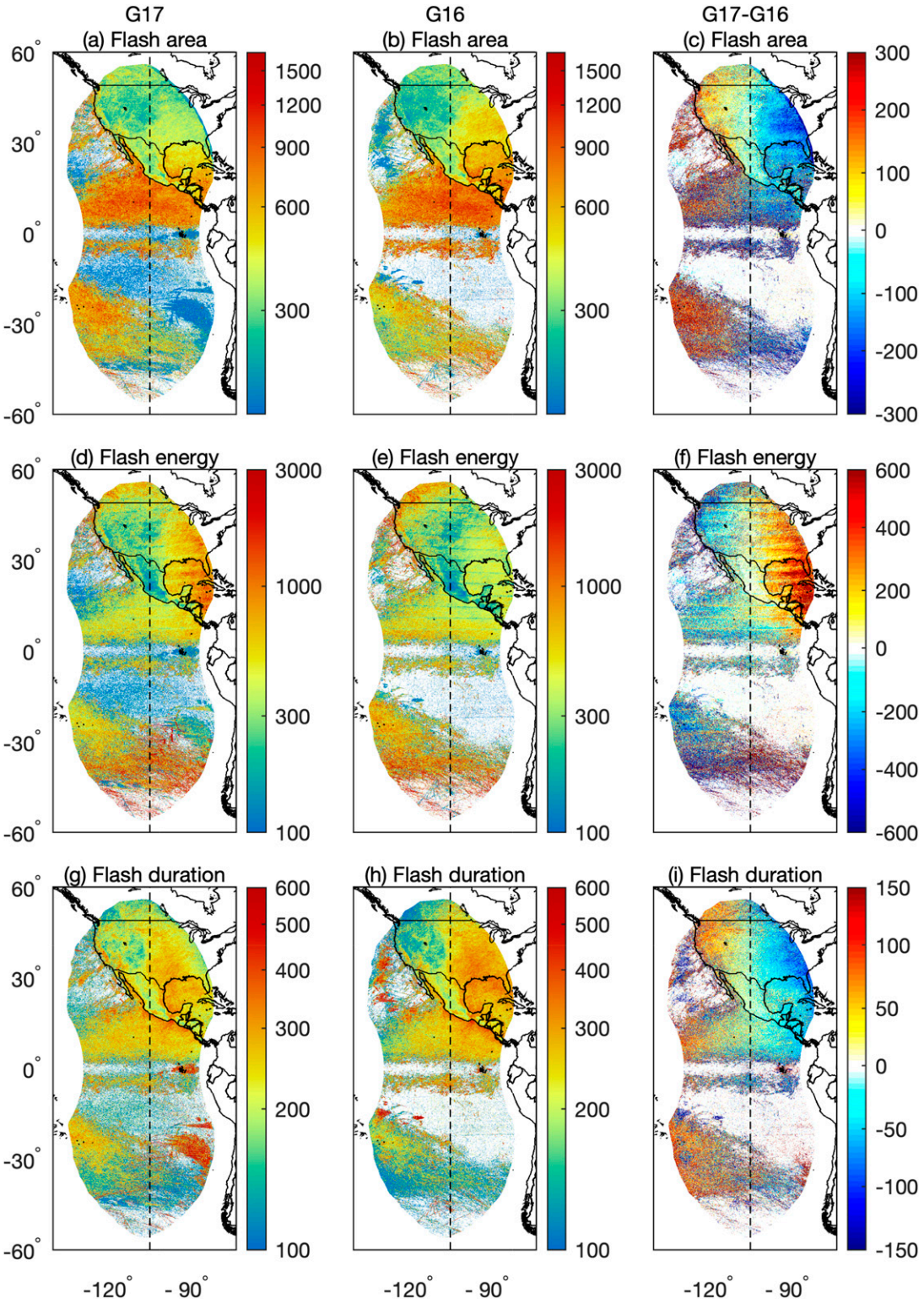

FIG. 3. Region of overlapping coverage between the *G17* and *G16* GLMs: (a) *G17* average flash area, (b) *G16* average flash area, (c) difference between average flash area *G17* minus *G16*, (d) *G17* average flash energy, (e) *G16* average flash energy, (f) difference between average flash energy *G17* minus *G16*, (g) *G17* average flash duration, (h) *G16* average flash duration, and (i) difference between average flash duration *G17* minus *G16*. Units are square kilometers for average flash area, femtojoules for average flash energy, and milliseconds for average flash duration. Stripes in the energy distributions [(d)–(f)] result from the first rows along the leading edges of subarray boundaries being more sensitive (termed overshoot). This pattern is most pronounced in (f) because the ground relative locations of these more sensitive rows do not match between *G16*/*G17*.

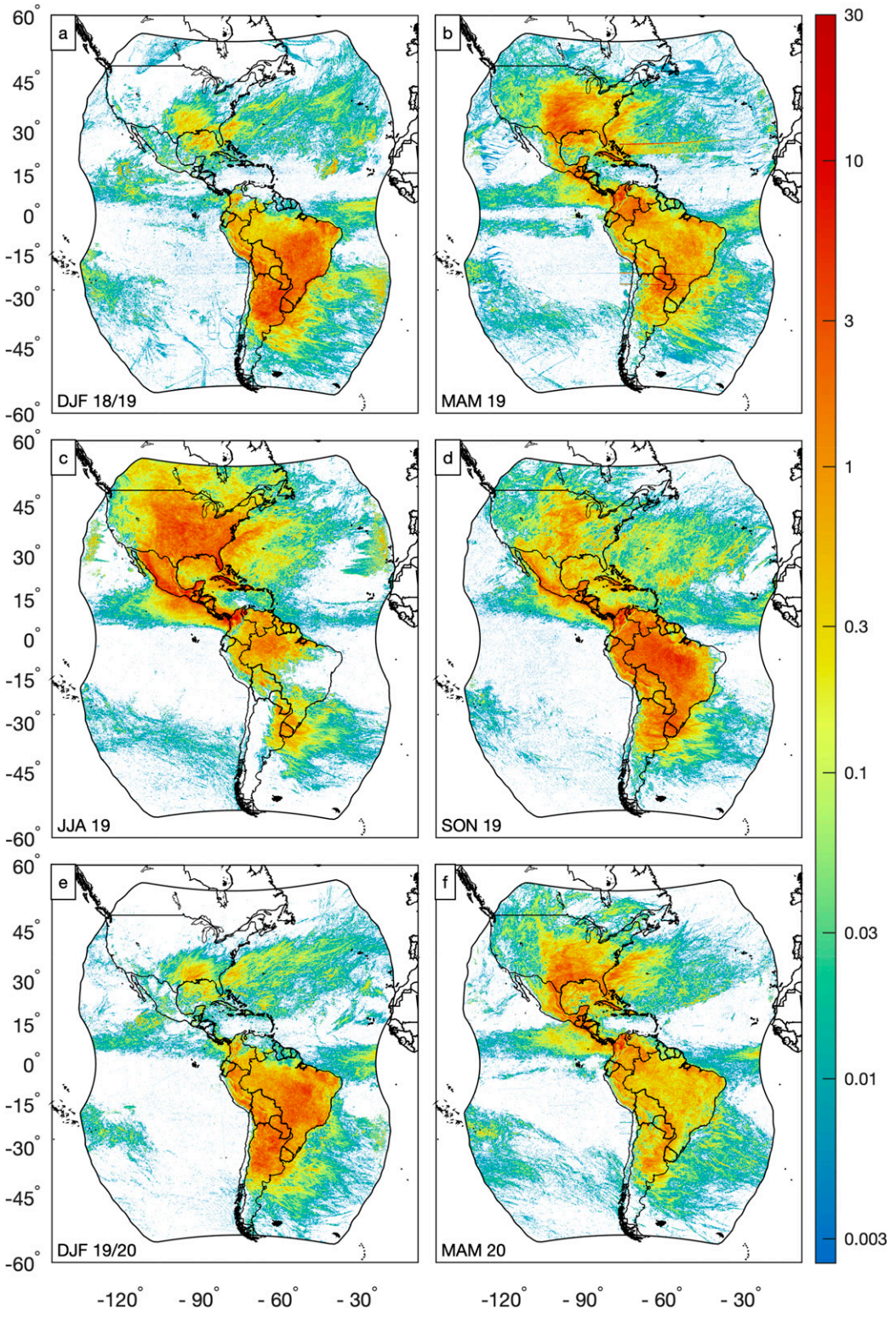

FIG. 4. Seasonal *G16* GLM flash densities with units of flash count per square kilometer per month. (a) December 2018–February 2019, (b) March–May 2019, (c) June–August 2019, (d) September–November 2019, (e) December 2019–February 2020, and (f) March–May 2020.

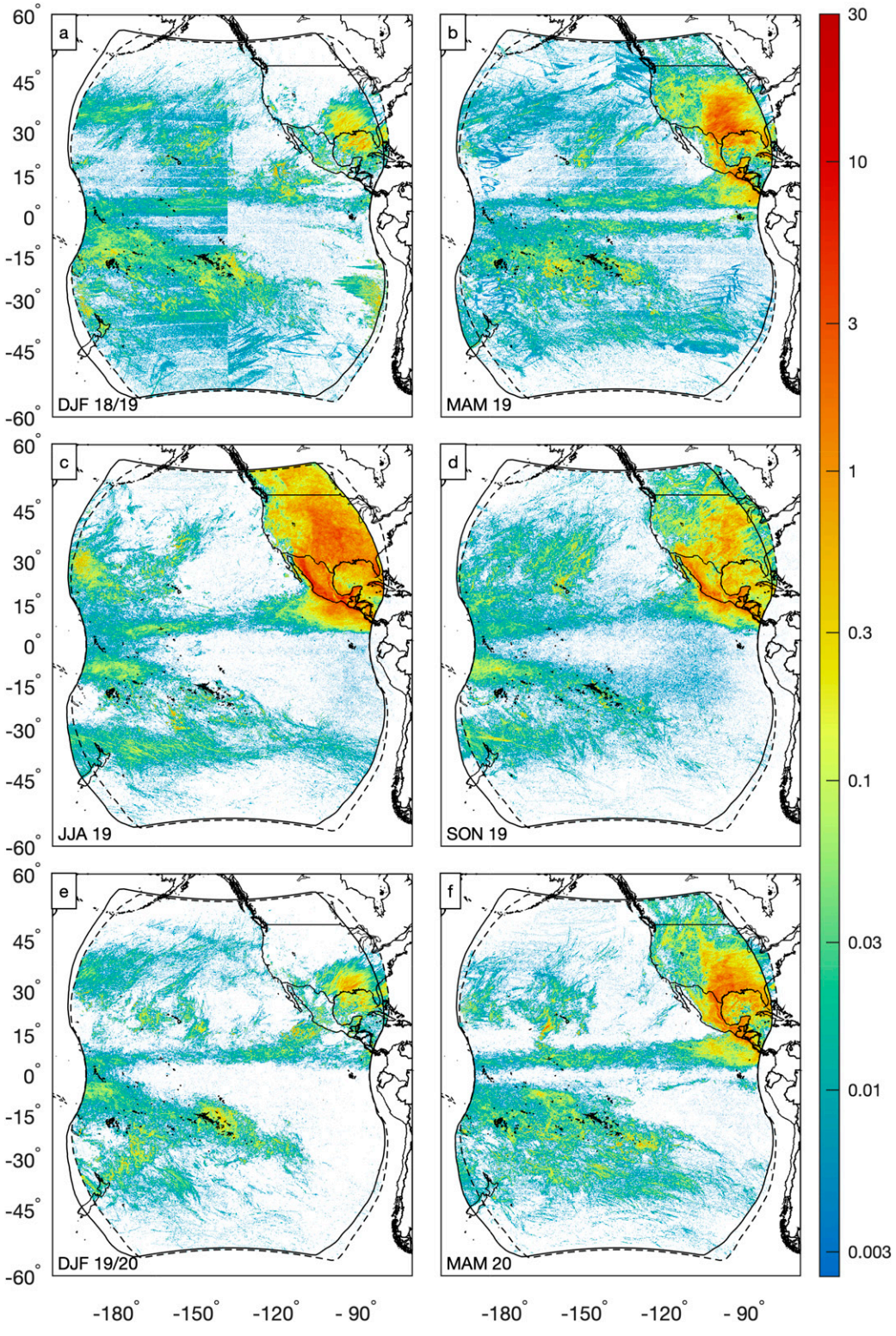

FIG. 5. As in Fig. 4, but for the *G17* GLM.

appearance during later seasons (JJA 2019, SON 2019, DJF 2019/20, and MAM 2020; Figs. 4c–f). The influence of the blooming filter (implemented on 25 July 2019, Table 1) appears when contrasting the impact of solar intrusion (high latitudes) and sun glint (mid- to low latitudes) during DJF 2018/19 versus DJF 2019/20 (Figs. 4a,e) and MAM 2019 versus MAM 2020 (Figs. 4b,f). During DJF 2019/20, many fewer false events appear over Canada and the North Atlantic, as well as the Pacific south of the equator (especially the western and eastern edges of the FOV). Improvements appear in similar regions during MAM, especially over the North Atlantic. During JJA 2019 (Fig. 4c), partial blooming filter coverage lessens the sun-glint artifacts along the eastern and western portions of the FOV in the Northern Hemisphere. Although solar intrusion and sun glint still occur, the blooming filter prevents cascades of false events, resulting in greatly diminished artifacts. The second-level threshold filter provided the second most impactful improvement during the study period (install completed on 30 April 2019, Table 1). The ''Bahamas Bar'' artifact, depicted by a streak of enhanced flash densities during MAM 2019 (Fig. 4b), is almost indistinguishable during MAM 2020 (Fig. 4f). Bar artifacts occur when bright clouds persist along particular subarray boundaries near solar noon (i.e., high sun angles). There is no perfect solution to the bar artifacts, and tuning the second level threshold filter involves a give and take. Certain conditions will continue to produce false flashes, coupled with an inverse effect where flash densities are diminished along the same boundaries under the same solar angle and cloud conditions (i.e., slow-moving clouds near solar noon).

The *G17* GLM exhibits similar improvements to the *G16* GLM, along with two *G17* specific improvements. The blooming and second level threshold filters diminish solar intrusion and sun-glint artifacts in similar FOV-relative locations for the *G16* and *G17* GLMs. Sun-glint artifacts along the southeastern edge of the FOV during DJF 2018/19 (Fig. 5a) nearly disappear during DJF 2019/20 (Fig. 5e). Solar intrusion artifacts over the northern Pacific during MAM 2019 (Fig. 5b) greatly diminish during MAM 2020 (Fig. 5f). Overall noisier patterns in Fig. 5 (versus Fig. 4) reveal less mature *G17* GLM ground system settings, but also suggest the *G17* GLM is slightly more sensitive than the *G16* GLM. Despite the *G17* GLM reaching provisional maturity in December 2019, fine tuning continued through the study period. The striped patterns apparent in Figs. 5a and 5b were removed by fine tuning the electronic timing parameters, enabling the contrast leakage filter, and adjusting the second level threshold filter. The two halves of the GLM CCD (a split frame-transfer device) have separately controlled timing parameters that were selected during ground testing to balance a number of performance criteria, including noise. The *G17* GLM had slightly more noise in one-half of the CCD, especially on scene contrast boundaries (e.g., cloud edges). These false alarms were suppressed by enabling the contrast leakage filter and fine-tuning the second level threshold parameters. Disturbances to platform stability related to spacecraft navigation and instrument calibration scans can trigger many false GLM events along cloud edges during daytime. Although changes to onboard settings are rare, the background clamp values were modified on 15 October 2019 to slightly reduce sensitivity and help mitigate false flashes associated with a long-term (4+ month) space-weather instrument calibration scan. This improvement appears when comparing Fig. 5d (before) with Fig. 5e (after), especially in the eastern Pacific.

Our focus now shifts to documenting seasonal variability throughout the broad GLM coverage area. Figure 4 depicts the most recent seasonal cycle observed by the *G16* GLM (June 2019–May 2020; Figs. 4c–f), showing lightning activity shift from north to south and back. The observed seasonal patterns closely match those described by Cecil et al. (2014; their Fig. 3) and Albrecht et al. (2016, their Figs. 1c, 3b). The continents dominate during each season, although widespread lightning also occurs over the Atlantic Ocean year-round. In North America, lightning activity clearly peaks during JJA (Fig. 4c), with a pronounced minimum during DJF (Figs. 4a,e). In South America, comparably large flash density values occur during SON (Fig. 4d) and DJF (Figs. 4a,e). An exception occurs in Colombia and Venezuela, where local flash densities exceed 10 flashes km^{-2} $month^{-1}$ in each season except DJF. This DJF minima relates to a strengthening Caribbean low level jet stream, which increases shear and suppresses convection (Muñoz et al. 2016; Hidalgo et al. 2015). Seasonal lightning distributions in North America generally agree between the *G16* (Fig. 4) and *G17* GLMs (Fig. 5).

Despite lower flash densities, interesting features occur over the Pacific Ocean (Fig. 5). Fewer studies describe the seasonal lightning patterns visible to the *G17* GLM, with most focusing on sub regions (e.g., Pessi and Businger 2009; Liu et al. 2012; Virts et al. 2013; Bang and Zipser 2019). The *G17* GLM provides the first continuous total lightning coverage over much of the Pacific. Figure 5 reveals three oceanic regions with lightning in each season that demonstrate the key role convective organization plays in producing lightning over the oceans. Figure 6 illustrates seasonal time series for these three regions. The greatest flash densities over the open Pacific Ocean occur in a region stretching from the west Pacific warm pool southeastward to French Polynesia. Ortéga and Guignes (2007) documented the importance of the South Pacific Convergence Zone (SPCZ) in producing year-round lightning in this region with a peak during March. Figure 5 also indicates year-round lightning in this region, and Fig. 6f reveals the March peak. The monthly flash densities in the SPCZ region remain >0.045 flashes km^{-2} $month^{-1}$ throughout the year, exceeding even the peaks in the other two regions. Within the central North Pacific (15°–40°N, 140°W–180°), lightning activity peaks during November with a minimum during May (Fig. 6b). During winter, Pessi and Businger (2009) found most electrical activity in this region to be associated with cold fronts and extratropical cyclones. The summer cases were mostly triggered by cold upper-tropospheric disturbances associated with a tropical upper-tropospheric trough (TUTT).

Evidence of the Pacific intertropical convergence zone (ITCZ) appears throughout the year as an east–west band just north of the equator (Figs. 4 and 5). The relative lack of lightning directly over the equator illustrates the importance of the underlying sea surface temperatures (SSTs) on lightning occurrence over the oceans. The seasonal meridional migration of

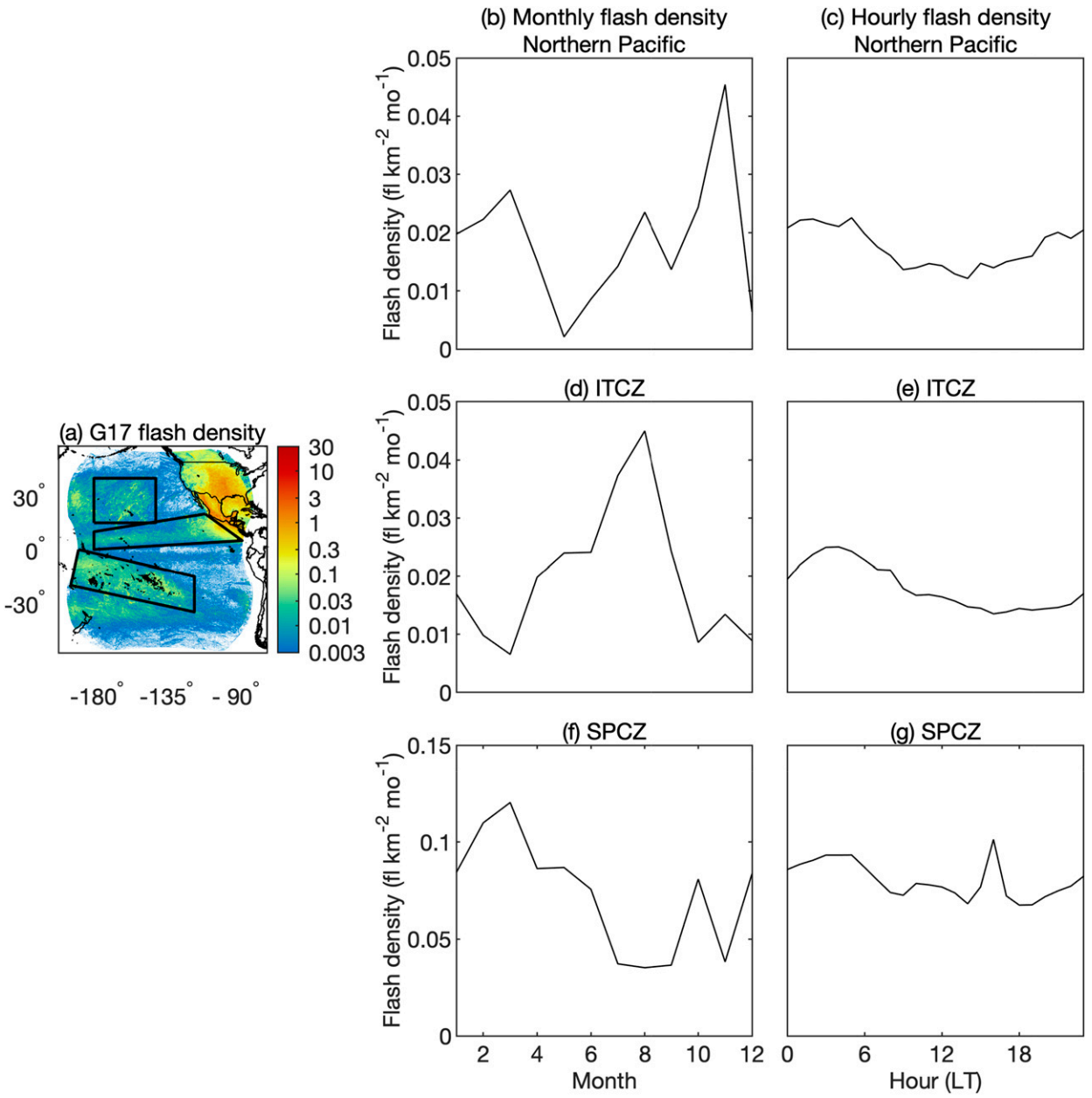

FIG. 6. (b),(d),(f) Monthly and (c),(e),(g) hourly flash density time series within the central North Pacific, intertropical convergence zone (ITCZ), and South Pacific convergence zone (SPCZ). The three regions are indicated by thick black lines overlaid on the (a) *G17* GLM flash densities. Note the different scale for (f) and (g).

warm SSTs dictates the percentage coverage of deep convection within different latitudinal bands (Mitchell and Wallace 1992). Throughout most of the year in the Pacific Ocean, the warm waters are north or south of the equator (mostly north), split by a zone of equatorial ocean upwelling (i.e., cool equatorial SSTs; Waliser and Jiang 2015; Mitchell and Wallace 1992). Over the western-central Pacific, Chen et al. (2008) showed that ITCZ deep convection occurs over the equator only 8.3% of the time. Figure 6d reveals a strong seasonal cycle in the Pacific ITCZ region with peak lightning activity during JJA. This seasonal maximum is likely dominated by thunderstorm systems that initiate over Central America and propagate westward (see section 3c), with some contribution from tropical cyclones. During boreal winter, such storms are rare as evidenced by the low lightning densities from southern Mexico to Costa Rica and areas immediately offshore (Figs. 5a,e). Wodzicki and Rapp (2016) found that the Pacific ITCZ has narrowed and its associated convection has intensified, highlighting the importance of continued GLM observation of these important climatological features.

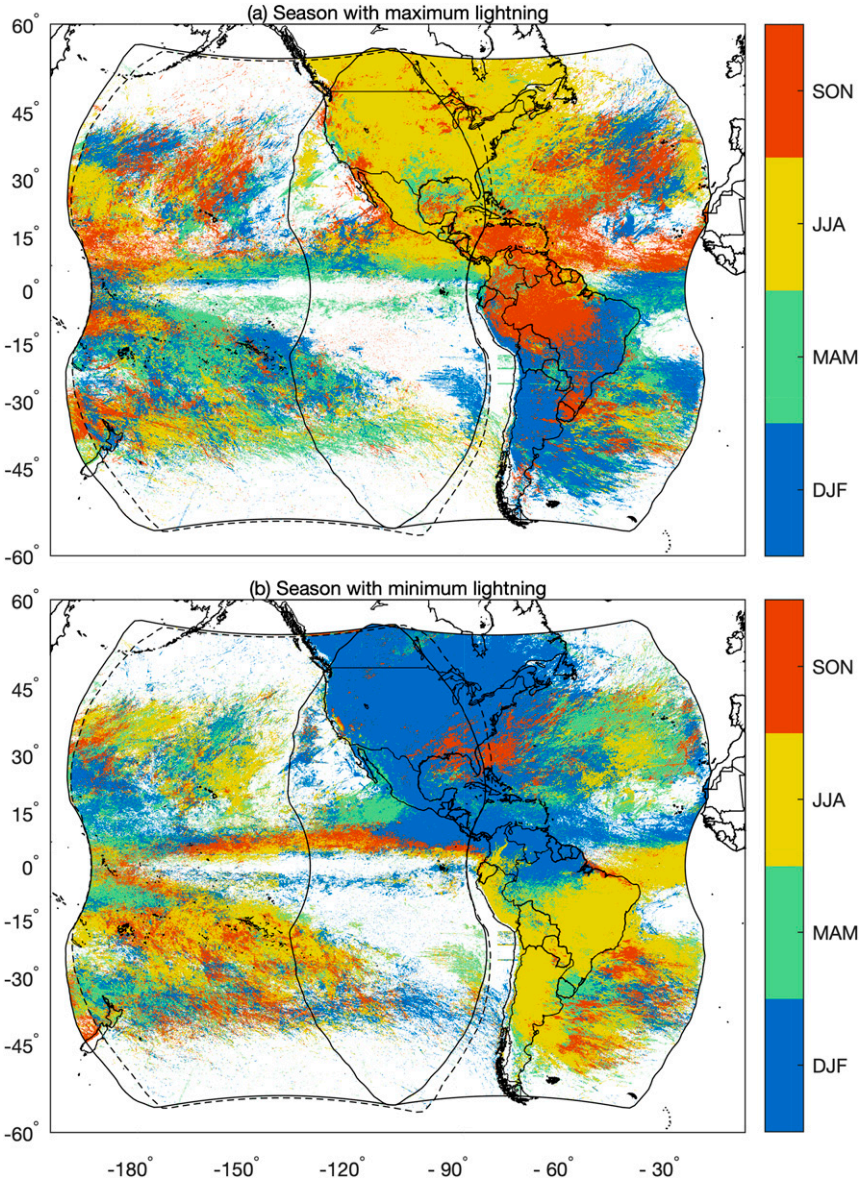

FIG. 7. Season of (a) maximum and (b) minimum lightning flash density for the combined *G16*/*G17* GLM field of view.

Figure 7 depicts the seasons with maximum and minimum lightning activity to illustrate important natural variability. Seasonal patterns again match those shown by Albrecht et al. (2016; their Fig. 1c). In North America, lightning peaks during JJA (Fig. 7a), with a few noteworthy exceptions. Lightning activity peaks during MAM in parts of the southern United States and northern Gulf of Mexico, and during SON in some regions near the Great Lakes and along the California–Mexico border. In South America, lightning activity generally peaks during SON (DJF) to the north (south) of 15°S. Exceptions occur over Paraguay (MAM), eastern Brazil (DJF), far southern Brazil and Uruguay (SON), and scattered areas along the northern coast of South America (JJA). New Zealand presents a unique situation with a DJF maximum over land and JJA/SON (local winter/spring) maxima over oceanic areas to the north and east. Seasonal cycles are less defined over the oceans. The influence of storm systems with continental origins appears as a mix of MAM and JJA maxima off the east coast of North America that transition to SON/DJF maxima farther offshore. Most places exhibit opposite minimum (Fig. 7b) and maximum seasons (e.g., many regions with JJA maxima and DJF minima). North (south) of the equator, DJF (JJA) minima are most widespread, although interesting exceptions are observed over California and the central Pacific ITCZ with JJA/SON minima. As more data become available, future studies are encouraged to examine exceptions to these general trends.

Seasonal time series in the overlapping coverage region provide additional context for the spatial plots (Fig. 8). The

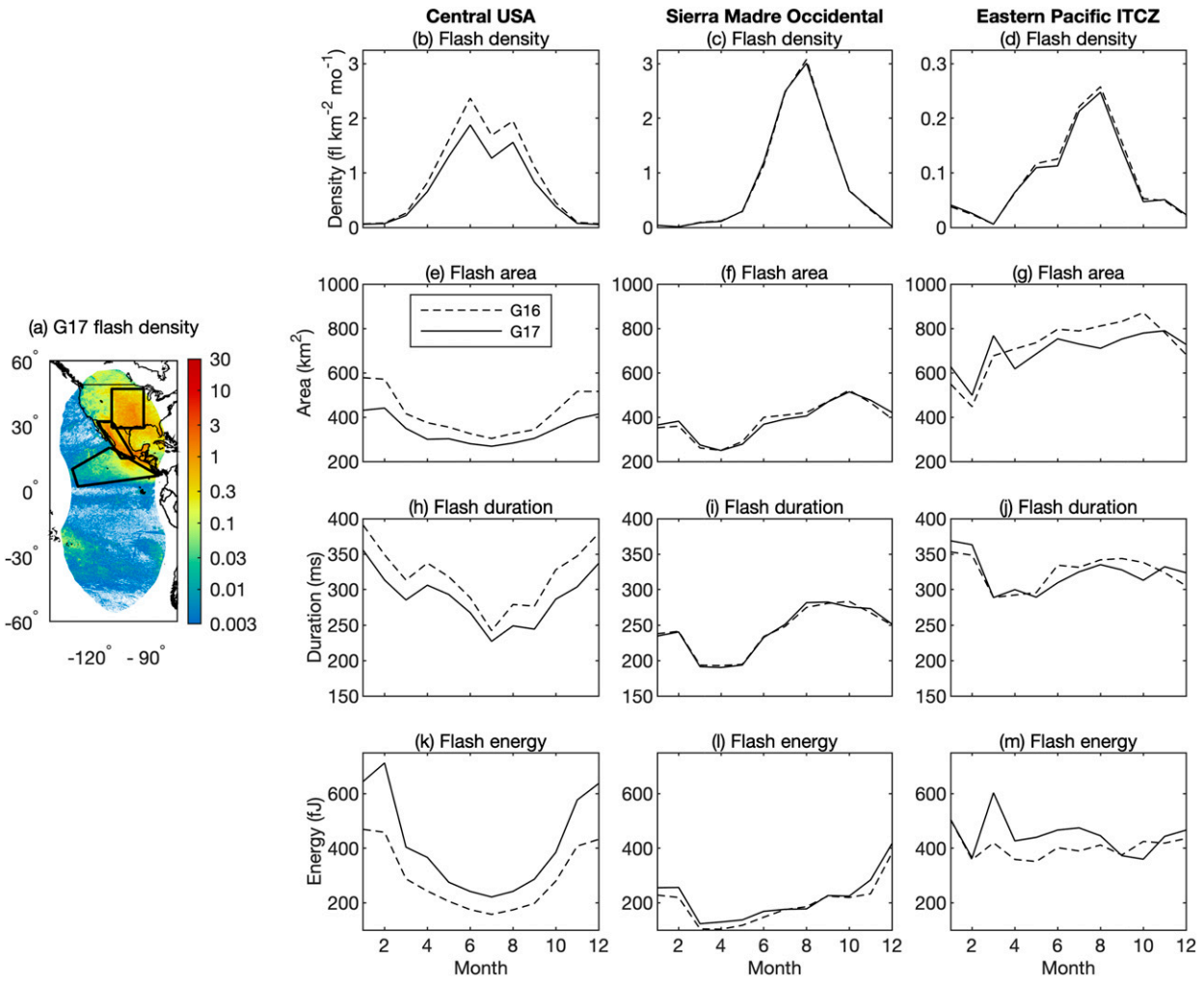

FIG. 8. *G16* and *G17* GLM monthly time series of average (b)–(d) flash density, (e)–(g) area, (h)–(j) duration, and (k)–(m) energy for the (left) central United States, (center) the Sierra Madre Occidental, and (right) the eastern Pacific intertropical convergence zone. The three regions are indicated by thick black lines overlaid on the (a) *G17* GLM flash densities for the overlap region. Note the different scale for (d) [vs (b) and (c)].

G16 and *G17* GLMs observe similar seasonal trends in average flash density (Figs. 8b–d), area (Figs. 8e–g), duration (Figs. 8h–j), and energy (Figs. 8k–m) when categorized by region. Along with the trends, the magnitudes of the *G16* and *G17* values agree well in the Sierra Madre Occidental (center panels) and the eastern Pacific ITCZ (right panels). Despite similar trends, the magnitudes of the *G16* and *G17* GLM values differ in the central United States (left panels). In the central United States, *G17* GLM flashes are less frequent, smaller, shorter duration, and more energetic than *G16* flashes. This reflects expected effects nearer the edge of the *G17* FOV, but may also include some natural variability.

Seasonal cycles vary between regions and GLM parameters. Flash densities exhibit pronounced seasonal cycles in each region with maxima during JJA (Figs. 8b–d). Flash densities are an order of magnitude lower in the eastern Pacific ITCZ (Fig. 8d). Seasonal cycles in flash duration and energy are most pronounced in the central United States, which exhibits weaker, shorter-duration flashes on average during summer. Over the central United States, average flash energy (duration) values range from 500 to 700 fJ (>325 ms) during winter to values of 150–250 fJ (<250 ms) during summer. The Sierra Madre Occidental exhibits minima in both average flash area and duration during MAM (Figs. 8f,i). The average flash duration over the Sierra Madre Occidental increases during summer and fall, before decreasing again during winter toward a spring minimum. This indicates more frequent upscale growth into MCSs during the summer and fall, consistent with increased offshore propagation appearing in Figs. 5c and 5d. The eastern Pacific ITCZ exhibits relatively large, long-duration flashes throughout the year, with some less obvious seasonal variability. As these distributions become better documented, future studies should work to incorporate GLM information beyond flash frequency into climatological applications.

c. *Diurnal variability*

Rudlosky et al. (2019) noted an innovative aspect of the GLM is the ability to continuously detect lightning at every location within its near-hemispheric FOV. By tracking total lightning distributions throughout the diurnal cycle at every location, 18 months of GLM observations reveal distributions very similar to those shown using 16 years of TRMM/LIS observations (Albrecht et al. 2016; their Fig. 1b). To simplify the diurnal cycle, which can be noisy given the relatively short analysis period, harmonic analysis is performed on the hourly lightning densities at each location throughout the combined FOV. In this analysis, the diurnal cycle at each location is reconstructed by combining harmonics 1–3 of the hourly lightning, thus retaining the primary characteristics of the hourly lightning densities. Figure 9 shows the local hour when combined harmonics 1–3 are at their maximum/minimum. Most land areas (including islands) exhibit afternoon maxima (Fig. 9a), with some noteworthy exceptions. Narrow land features such as Baja California and Panama exhibit earlier maxima (near local noon), while a maximum near midnight occurs over the extreme eastern perimeter of Mexico, east of the Sierra Madre Occidental. Sea-breeze circulations result in pronounced afternoon maxima over Florida, Cuba, and Central America. Nocturnal offshore maxima are observed over the Gulf of Mexico and around Central America, where phase propagation away from land is evident. Inland propagation of sea-breeze-initiated thunderstorms into the evening and nighttime hours appears over northeastern South America.

Contrasting the diurnal cycles between regions provides important meteorological insights. The flash density diurnal cycle is less pronounced over the open oceans (Figs. 6c,e,g and 10d) than over land (Figs. 8b,c and 10b,c). Subtle nocturnal flash density maxima appear in the northern Pacific and ITCZ regions (Figs. 6c,e). The SPCZ flash density maxima occurs at 1600 LT, with a secondary peak in the early morning (i.e., 0300–0500 LT). These diurnal maxima match the timing of the minimum infrared brightness temperatures (indicative of the strongest storms) shown by Haffke and Magnusdottir (2015). Lightning activity peaks earlier in the day (nearer local noon) above the Rocky (Andes) Mountains than other parts of North (South) America (Fig. 9a). The diurnal flash density maximum over the Sierra Madre Occidental peaks ~1 h earlier than over the central United States and is sharper/narrower above this steeper terrain (Figs. 10b,c). Nocturnal minima occur along the Andean foothills coincident with frequent mountain breeze convergence (Fig. 9b). Nocturnal maxima over parts of the Great Plains and northern Argentina reflect the prevalence of upscale growth into MCSs in these regions. Orville and Huffines (2001) found lightning activity in the upper Great Plains peaks between 2000 and 0400 LT. Several studies have related unusual CG lightning characteristics in this region (e.g., Carey and Buffalo 2007) to the frequent occurrence of nocturnal MCSs (Geerts et al. 2017). During austral summer, Rasmussen et al. (2014) found that hail and lightning concentrate over the foothills of western Argentina and that lightning has a nocturnal maximum associated with storms having deep mesoscale convective echoes. Nocturnal maxima also appear over Lake Maracaibo (as described by Albrecht et al. 2016), the Gulf of California, and midlatitude water bodies such as the southern Hudson Bay, near the Great Lakes, and portions of the Gulf of St. Lawrence.

Many places exhibit a ~12-h shift between the local hours with maximum/minimum lightning activity (Figs. 9a,b). Over most land areas, the minimum lightning activity typically occurs during early morning, with the Florida peninsula exhibiting a slightly earlier minimum around midnight. The Great Plains and Argentina again present exceptions, with lightning frequency minima around local noon. Evening minima occur over long stretches of the northeastern coast of South America. Over portions of the Andes and Central American terrain, the lightning minimum sometimes occurs just hours before the diurnal maximum. Patterns are more mixed over the oceans, with the proximity to land playing an important role. As previously shown, in the nearshore waters, the minimum lightning activity occurs during the peak of daytime heating.

Information beyond flash occurrence and frequency provides additional insights into storm type and evolution within certain regions. The *G16* and *G17* GLMs show similar diurnal trends in average flash area, duration, and energy within the individual regions (Fig. 10). As discussed in Fig. 3, mean flash properties differ for *G16* and *G17* over the central United States (Figs. 10e,h,k). Less frequent, smaller, shorter duration, more energetic *G17* flashes result from the proximity to the edge of the FOV, where larger pixels and steeper viewing angles reduce the instrument sensitivity. Despite differing magnitudes, the diurnal patterns match between instruments, further suggesting these differences relate to instrument detection artifacts rather than natural variability. Mean flash properties in the central United States exhibit similar diurnal timing to the Sierra Madre Occidental, but variations are generally smaller in magnitude, consistent with the notion of more diffuse diurnal variability over flatter terrain. Both sensors observed strong diurnal cycles in average flash area over the Sierra Madre Occidental (Fig. 10f) and especially over the eastern Pacific ITCZ (Fig. 10g), where values range from minima less than 500 km^2 during 0700–1700 local time (LT) to maxima greater than 900 km^2 during 1800–0600 LT. Pronounced diurnal variability exists in the average flash duration over the Sierra Madre Occidental (Fig. 10i), and to a lesser degree over the eastern Pacific ITCZ (Fig. 10j). Both regions also show minimum flash energy around noon (Figs. 10l,m). Nesbitt et al. (2008) documented an abrupt shallow to deep convective transition over the Sierra Madre Occidental, with shallow convective systems developing just before noon on average above the high peaks, and deep convection developing after 1500 LT on the western slopes. Our time series reveal initially small, short-duration GLM flashes growing larger and longer as storms grow upscale, shown by Nesbitt et al. (2008) to occur around 1900 LT. Their Fig. 9 indicated these storms transition offshore, where they likely contribute to the average flash area maxima over the eastern Pacific ITCZ (Figs. 3a,b and 10g).

4. Summary

This study examines observations from the *G16* and *G17* GLMs during the first 18 months of coincident coverage

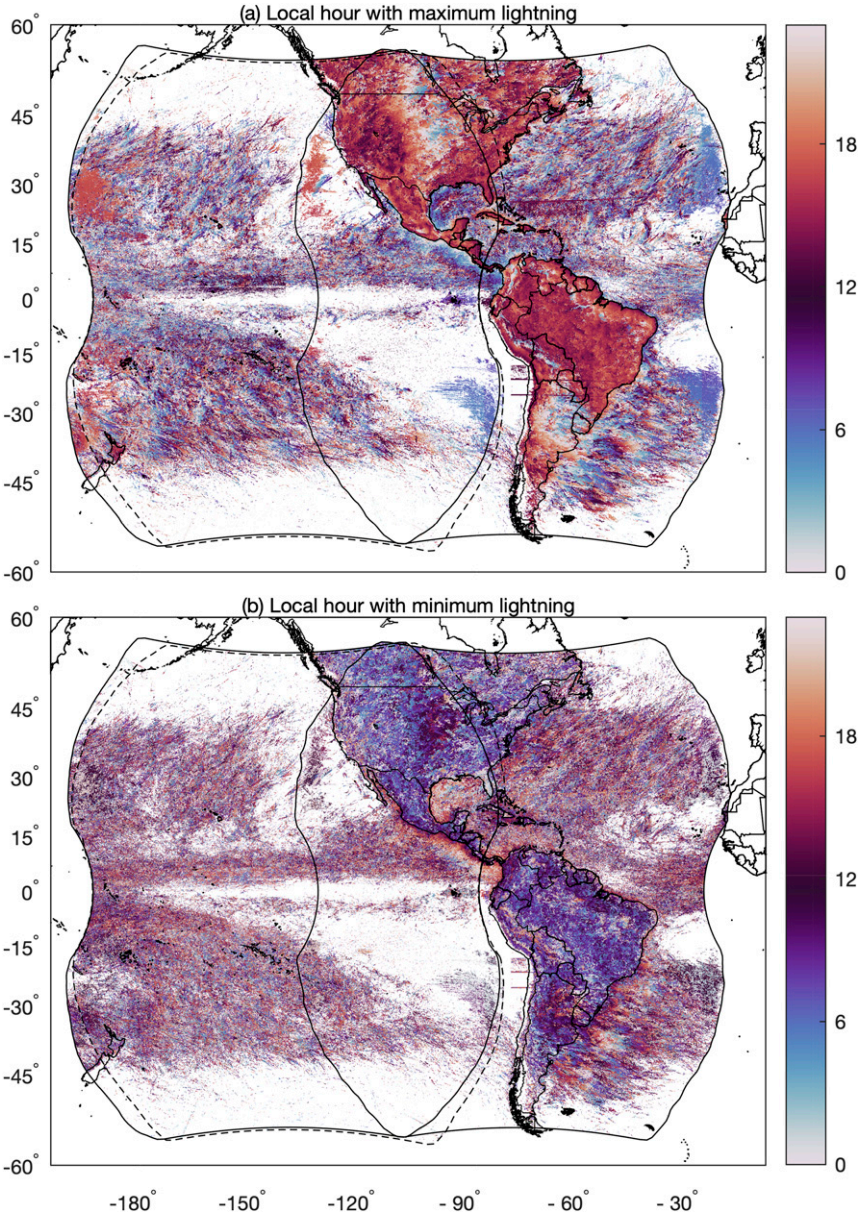

FIG. 9. Local hour with (a) maximum and (b) minimum lightning flash density for the combined *G16*/*G17* GLM field of view.

(1 December 2018–31 May 2020). The *G16* GLM covers most of the land areas in the Western Hemisphere, and detects ~4 times as much lightning as the *G17* GLM. The overall annual and seasonal patterns remain consistent with previous studies. Flash density values exceeding 1 flash km^{-2} $month^{-1}$ occur almost exclusively over land. The absolute lightning maximum for the combined GLM domain occurs in Venezuela and Colombia, where some locations experience more than 10 flashes km^{-2} $month^{-1}$ during each season except DJF. Relative maxima with >3 flashes km^{-2} $month^{-1}$ also appear over Florida, the Sierra Madre Occidental, and Cuba. The sharpest flash density contrasts coincide with coastlines and mountain ranges.

Lightning occurs much less frequently offshore. The MCSs responsible for much of the lightning over North and South America appear to contribute to relative maxima downwind of both continents. The influence of the Gulf Stream appears as a pronounced region of enhanced flash densities east of North America. Land–sea lightning contrasts appear beyond flash density distributions. Results suggest that the tendency for oceanic lightning to occur within larger, longer lasting, and more organized storm systems contributes to the larger, longer-lasting, and more energetic GLM flashes observed over ocean by both sensors.

Overlapping observations reveal similarities and differences between the *G16* and *G17* GLM observations. The overall

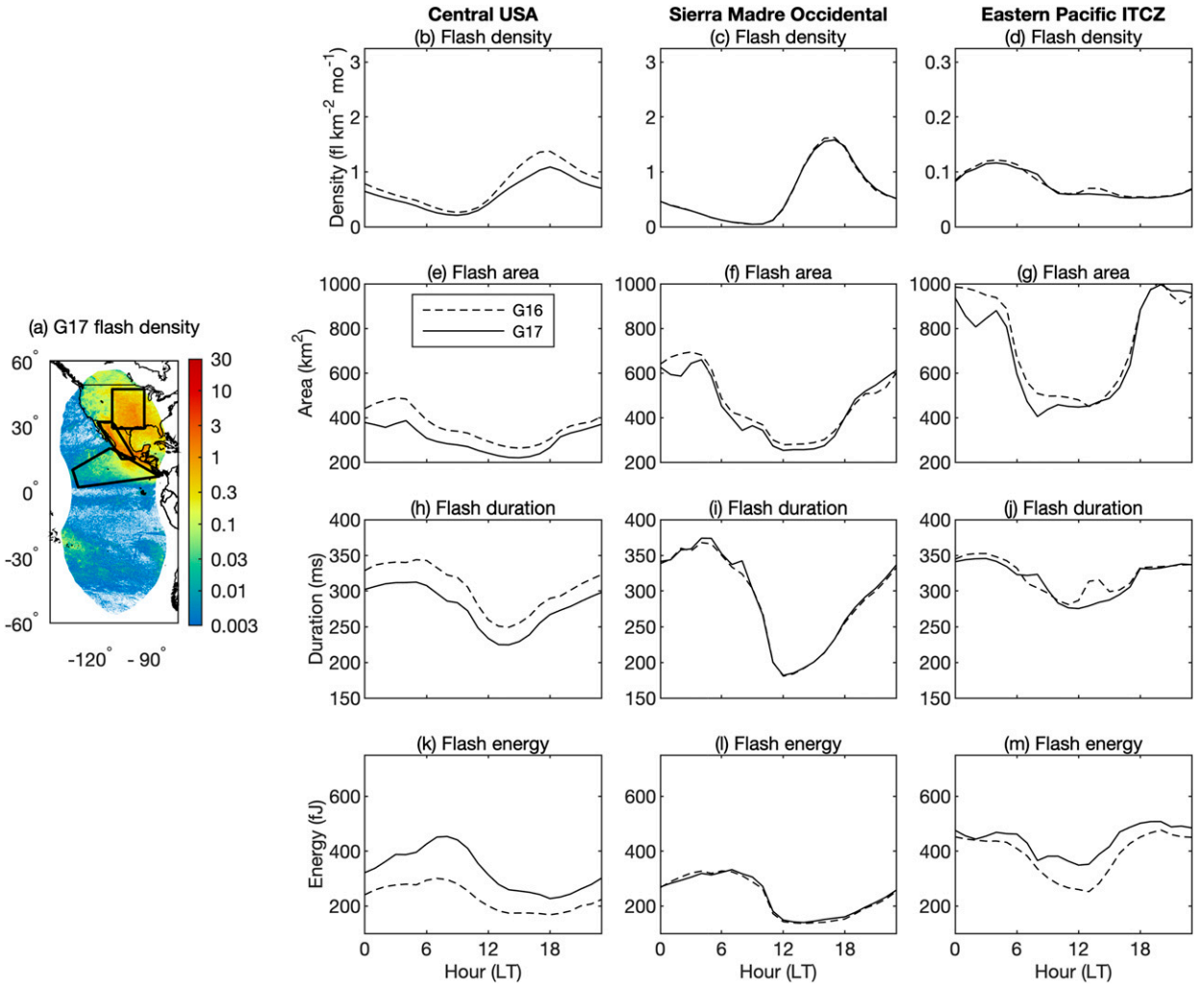

FIG. 10. *G16* and *G17* GLM hourly time series of average (b)–(d) flash density, (e)–(g) area, (h)–(j) duration, and (k)–(m) energy for the (left) central United States, (center) the Sierra Madre Occidental, and (right) the eastern Pacific intertropical convergence zone. The three regions are indicated by thick black lines overlaid on the (a) *G17* GLM flash densities for the overlap region. Note the different scale for (d) [vs (b) and (c)].

spatial flash density patterns generally agree between the *G16* and *G17* GLMs, with a few important exceptions. Results show a north-south line near the center of the overlap region (~103°W), east (west) of which the *G16* (*G17*) GLM detects more lightning. For example, in the northwest United States, the *G16* GLM only observes 25%–45% of the *G17* GLM observed flashes. Reduced *G16* GLM performance in the northwest United States relates to the proximity to the edge of the FOV, where larger pixels and steeper viewing angles reduce the instrument sensitivity. Average flash energies (areas) are larger (smaller) near the edge of the FOV for each sensor.

Seasonal plots reveal diminishing GLM artifacts and improving data quality. Most GLM artifacts apparent during the first 6 months of the study period (December 2018–May 2019) greatly diminish during the final 6 months (December 2019–May 2020). The blooming (25 July 2019) and second-level threshold (30 April 2019) filters provided the greatest impacts. The second-level threshold filter helps mitigate bar artifacts, and the blooming filter quenches the rapid growth of both sunglint and solar intrusion artifacts. Although solar intrusion and sun glint still occur, the blooming filter prevents cascades of false events, resulting in greatly diminished artifacts.

The observed seasonal patterns closely match those described by previous studies, with the GLMs providing additional insights into these well-documented patterns. The continents dominate during each season, although widespread lightning also occurs year-round over portions of the Atlantic and Pacific Oceans. Over North America, lightning generally peaks during JJA. In South America, lightning activity generally peaks during SON (DJF) to the north (south) of 15°S. The *G17* GLM observed three regions over the Pacific with lightning in each season (i.e., central North Pacific, ITCZ, and SPCZ). These regions each demonstrate the key role

convective organization plays in producing lightning over the oceans. The greatest flash densities over the open Pacific are associated with the SPCZ in a region stretching from the west Pacific warm pool southeastward to French Polynesia.

The *G16* and *G17* GLMs observe similar seasonal trends in average flash density, area, duration, and energy when categorized by region. Seasonal cycles in average flash area, duration, and energy are most pronounced in the central United States, which exhibits smaller, shorter duration, and weaker flashes on average during summer. Despite similar seasonal trends, the magnitudes of the *G16* and *G17* GLM values differ in the central United States. In the central United States, *G17* GLM flashes are less frequent, smaller, shorter duration, and more energetic than *G16* flashes. As these distributions are better documented, future studies should focus on incorporating GLM information beyond flash frequency into climatological applications.

The GLMs allow total lightning distributions to be tracked throughout the diurnal cycle at any location within the combined FOV. Many places exhibit a ~12-h shift between the local hours with maximum/minimum lightning activity. Most land areas exhibit afternoon maxima and early morning minima, with some noteworthy exceptions. Sea-breeze circulations produce pronounced afternoon maxima over Florida, Cuba, and Central America. Diurnal patterns are more mixed over the oceans, with the proximity to land playing an important role. Nocturnal offshore maxima are observed over the Gulf of Mexico and around Central America, where phase propagation away from land is evident.

Texture within the flash densities reveals a close relationship with the underlying topography, underscored by the complex diurnal cycles observed along coastlines and in mountainous regions. Above portions of the Andes and Central American terrain, the diurnal lightning minimum sometimes occurs just hours before the diurnal maximum. Lightning activity peaks earlier in the day (nearer noon LT) over the Rocky (Andes) Mountains than other parts of North (South) America. The diurnal flash density maximum over the Sierra Madre Occidental peaks ~1 h earlier than over the central United States and is sharper/narrower above this steeper terrain. Nocturnal maxima appear over Lake Maracaibo, the Gulf of California, and several midlatitude water bodies.

Information beyond flash occurrence frequency provides additional insights into storm type and evolution within certain regions. Mean flash properties in the central United States exhibit similar diurnal timing to the Sierra Madre Occidental, but variations are generally smaller in magnitude, consistent with the notion of more diffuse diurnal variability above flatter terrain. The *G16* and *G17* GLMs observe strong diurnal cycles in average flash area and duration over the Sierra Madre Occidental and the eastern Pacific ITCZ. Pronounced diurnal variability exists in the average flash duration over the Sierra Madre Occidental, and to a lesser degree over the eastern Pacific ITCZ. Both regions show minimum flash energy around noon. Over the Sierra Madre Occidental, time series reveal initially small, short-duration GLM flashes growing larger and longer as storms grow upscale. These MCSs often transition offshore, contributing to the average flash area maxima over the eastern Pacific ITCZ.

High-resolution seasonal and diurnal lightning distributions reveal many features that merit future study as more GLM data become available. Compositing this information over many years will definitively describe both the seasonal and diurnal variability throughout the broad GLM coverage area.

Acknowledgments. The authors thank Steve Goodman, Eric Bruning, Rachel Albrecht, and two anonymous reviewers for their contributions to this manuscript. SR is funded by NESDIS/STAR and the GOES-R science program. KV is funded in part by the GOES-R Series Science, Demonstration, and Cal/Val Program at Marshall Space Flight Center. The contents of this paper are solely the opinions of the authors and do not constitute a statement of policy, decision, or position on behalf of NOAA or the U.S. government.

Data availability statement. GOES-R GLM data are publically available via the NOAA Comprehensive Large Array-data Stewardship System (CLASS) at https://www.bou.class.noaa.gov/saa/products/search?datatype_family=GRGLMPROD.

REFERENCES

Albrecht, R. I., C. A. Morales, and M. A. F. Silva Dias, 2011: Electrification of precipitating systems over the Amazon: Physical processes of thunderstorm development. *J. Geophys. Res.*, **116**, D08209, https://doi.org/10.1029/2010JD014756.

——, S. J. Goodman, D. E. Buechler, R. J. Blakeslee, and H. J. Christian, 2016: Where are the lightning hotspots on Earth? *Bull. Amer. Meteor. Soc.*, **97**, 2051–2068, https://doi.org/10.1175/BAMS-D-14-00193.1.

Bang, S. D., and E. Zipser, 2019: Tropical oceanic thunderstorms near Kwajalein and the roles of evolution, organization, and forcing in their electrification. *J. Geophys. Res. Atmos.*, **124**, 544–562, https://doi.org/10.1029/2018JD029320.

Barrett, B. S., and S. Hameed, 2017: Seasonal variability in precipitation in central and southern Chile: Modulation by the South Pacific high. *J. Climate*, **30**, 55–69, https://doi.org/10.1175/JCLI-D-16-0019.1.

Bateman, M., and D. Mach, 2020: Preliminary detection efficiency and false alarm rate assessment of the Geostationary Lightning Mapper on the *GOES-16* satellite. *J. Appl. Remote Sens.*, **14**, 032406, https://doi.org/10.1117/1.JRS.14.032406.

Bitzer, P. M., 2017: Global distribution and properties of continuing current in lightning. *J. Geophys. Res. Atmos.*, **122**, 1033–1041, https://doi.org/10.1002/2016JD025532.

Boccippio, D. J., S. J. Goodman, and S. Heckman, 2000: Regional differences in tropical lightning distributions. *J. Appl. Meteor.*, **39**, 2231–2248, https://doi.org/10.1175/1520-0450(2001)040<2231:RDITLD>2.0.CO;2.

Bruning, E. C., and D. R. MacGorman, 2013: Theory and observations of controls on lightning flash size spectra. *J. Atmos. Sci.*, **70**, 4012–4029, https://doi.org/10.1175/JAS-D-12-0289.1.

——, and Coauthors, 2019: Meteorological imagery for the Geostationary Lightning Mapper. *J. Geophys. Res. Atmos.*, **124**, 14 285–14 309, https://doi.org/10.1029/2019JD030874.

Burleyson, C. D., Z. Feng, S. M. Hagos, J. Fast, L. A. T. Machado, and S. T. Martin, 2016: Spatial variability of the background diurnal cycle of deep convection around the GoAmazon2014/5 field campaign sites. *J. Appl. Meteor. Climatol.*, **55**, 1579–1598, https://doi.org/10.1175/JAMC-D-15-0229.1.

Carey, L. D., and K. M. Buffalo, 2007: Environmental control of cloud-to-cround lightning polarity in severe storms. *Mon. Wea. Rev.*, **135**, 1327– 1353, https://doi.org/10.1175/MWR3361.1.

Cecil, D. J., D. E. Buechler, and R. J. Blakeslee, 2014: Gridded lightning climatology from TRMM-LIS and OTD: Dataset description. *Atmos. Res.*, **135–136**, 404–414, https://doi.org/10.1016/j.atmosres.2012.06.028.

——, ——, J. R. Mecikalski, and X. Li, 2020: Rapid scan visible imagery from the Geostationary Lightning Mapper (GLM) at 2.5-minute intervals. *Mon. Wea. Rev.*, **148**, 5105–5112, https://doi.org/10.1175/MWR-D-20-0079.1.

Chen, B., X. Lin, and J. T. Bacmeister, 2008: Frequency distribution of daily ITCZ patterns over the western–central Pacific. *J. Climate*, **21**, 4207–4222, https://doi.org/10.1175/2008JCLI1973.1.

Christian, H. J., and Coauthors, 2003: Global frequency and distribution of lightning as observed from space by the optical transient detector. *J. Geophys. Res.*, **108**, 4005, https://doi.org/10.1029/2002JD002347.

Cummins, K. L., and M. J. Murphy, 2009: An overview of lightning locating systems: History, techniques, and data uses, with an in-depth look at the U.S. NLDN. *IEEE Trans. Electromagn. Compat.*, **51**, 499–518, https://doi.org/10.1109/TEMC.2009.2023450.

dos Santos, M. J., F. Silva, M. A. Dias, and E. D. Freitas, 2014: Influence of local circulations on wind, moisture, and precipitation close to Manaus City, Amazon Region, Brazil. *J. Geophys. Res. Atmos.*, **119**, 13 233–13 249, https://doi.org/10.1002/2014JD021969.

Edgington, S., C. Tillier, and M. Anderson, 2019: Design, calibration, and on-orbit testing of the Geostationary Lightning Mapper on the GOES-R series weather satellite. *Proc. SPIE*, **11180**, 1118040, https://doi.org/10.1117/12.2536063.

Fierro, A. O., S. Stevenson, and R. Rabin, 2018: Evolution of GLM observed total lightning in Hurricane Maria (2017) during the period of maximum intensity. *Mon. Wea. Rev.*, **146**, 1641–1666, https://doi.org/10.1175/MWR-D-18-0066.1.

——, Y. Wang, J. Gao, and E. R. Mansell, 2019: Variational assimilation of radar data and GLM lightning-derived water vapor for the short-term forecasts of high-impact convective events. *Mon. Wea. Rev.*, **147**, 4045–4069, https://doi.org/10.1175/MWR-D-18-0421.1.

Garreaud, R., and R. C. Muñoz, 2005: The low-level jet off the west coast of subtropical South America: Structure and variability. *Mon. Wea. Rev.*, **133**, 2246–2261, https://doi.org/10.1175/MWR2972.1.

Geerts, B., and Coauthors, 2017: The 2015 Plains Elevated Convection At Night field project. *Bull. Amer. Meteor. Soc.*, **98**, 767–786, https://doi.org/10.1175/BAMS-D-15-00257.1.

GOES-R Algorithm Working Group, 2017: GOES R Series product definition and users' guide. Vol. 3, 416-R-PUG-L1B-0347, Level 1B products, 442 pp., https://www.goes-r.gov/users/docs/PUG-L1b-vol3.pdf.

Goss, H., 2020: Lightning research flashes forward. *Eos, Trans. Amer. Geophys. Union*, **101**, https://doi.org/10.1029/2020EO142805.

Haffke, C., and G. Magnusdottir, 2015: Diurnal cycle of the South Pacific Convergence Zone in 30 years of satellite images. *J. Geophys. Res. Atmos.*, **120**, 9059–9070, https://doi.org/10.1002/2015JD023436.

Hidalgo, H. G., A. M. Durán-quesada, J. A. Amador, and E. J. Alfaro, 2015: The Caribbean low-level jet, the inter-tropical convergence zone and precipitation patterns in the intra-Americas sea: A proposed dynamical mechanism. *Geografiska Ann.*, **97**, 41–59, https://doi.org/10.1111/geoa.12085.

Hu, J., A. O. Fierro, Y. Wang, J. Gao, and E. R. Mansell, 2020: Exploring the assimilation of GLM-derived water vapor mass in a cycled 3DVAR framework for the short-term forecasts of high-impact convective events. *Mon. Wea. Rev.*, **148**, 1005–1028, https://doi.org/10.1175/MWR-D-19-0198.1.

Hutchins, M. L., R. H. Holzworth, J. B. Brundell, and C. J. Rodger, 2012: Relative detection efficiency of the world wide lightning location network. *Radio Sci.*, **47**, RS6005, https://doi.org/10.1029/2012RS005049.

Jenniskens, P., and Coauthors, 2018: Detection of meteoroid impacts by the Geostationary Lightning Mapper on the GOES-16 satellite. *Meteor. Planet. Sci.*, **53**, 2445–2469, https://doi.org/10.1111/maps.13137.

Kong, R., M. Xue, A. O. Fierro, Y. Jung, C. Liu, E. R. Mansell, and D. R. MacGorman, 2020: Assimilation of GOES-R Geostationary Lightning Mapper flash extent density data in GSI EnKF for the analysis and short-term forecast of a mesoscale convective system. *Mon. Wea. Rev.*, **148**, 2111–2133, https://doi.org/10.1175/MWR-D-19-0192.1.

Lapierre, J., M. Hoekzema, M. Stock, C. Merrill, and S. C. Thangaraj, 2019: Earth Networks Lightning Network and Dangerous Thunderstorm Alerts. *2019 11th Asia-Pacific Int. Conf. on Lightning (APL)*, Hong Kong, IEEE, 1–5, https://doi.org/10.1109/APL.2019.8816032.

Liu, C., D. J. Cecil, E. J. Zipser, K. Kronfeld, and R. Robertson, 2012: Relationships between lightning flash rates and radar reflectivity vertical structures in thunderstorms over the tropics and subtropics. *J. Geophys. Res.*, **117**, D06212, https://doi.org/10.1029/2011JD017123.

Mach, D. M., 2020: Geostationary Lightning Mapper clustering algorithm stability. *J. Geophys. Res. Atmos.*, **125**, e2019JD031900, https://doi.org/10.1029/2019JD031900.

——, H. J. Christian, R. J. Blakeslee, D. J. Boccipio, and S. J. Goodman, and W. L. Boeck, 2007: Performance assessment of the optical transient detector and lightning imaging sensor. *J. Geophys. Res.*, **112**, D09210, https://doi.org/10.1029/2006JD007787.

——, R. J. Blakeslee, M. G. Bateman, and J. C. Bailey, 2010: Comparisons of total currents based on storm location, polarity, and flash rates derived from high-altitude aircraft overflights. *J. Geophys. Res.*, **115**, D03201, https://doi.org/10.1029/2009JD012240.

Machado, L. A. T., and Coauthors, 2018: Overview: Precipitation characteristics and sensitivities to environmental conditions during GoAmazon2014/5 and ACRIDICON-CHUVA. *Atmos. Chem. Phys.*, **18**, 6461–6482, https://doi.org/10.5194/acp-18-6461-2018.

Mitchell, T. P., and J. M. Wallace, 1992: The annual cycle in equatorial convection and sea surface temperature. *J. Climate*, **5**, 1140–1156, https://doi.org/10.1175/1520-0442(1992)005<1140:TACIEC>2.0.CO;2.

Muñoz, Á. G., J. Díaz-Lobatón, X. Chourio, and M. J. Stock, 2016: Seasonal prediction of lightning activity in North Western Venezuela: Large-scale versus local drivers. *Atmos. Res.*, **172–173**, 147–162, https://doi.org/10.1016/j.atmosres.2015.12.018.

Muñoz, R. C., and R. Garreaud, 2005: Dynamics of the low-level jet off the west coast of subtropical South America. *Mon. Wea. Rev.*, **133**, 3661–3677, https://doi.org/10.1175/MWR3074.1.

Murphy, M. J., and R. K. Said, 2020: Comparisons of lightning rates and properties from the U.S. National Lightning Detection Network (NLDN) and GLD360 with GOES-16 Geostationary Lightning Mapper and Advanced Baseline Imager data.

J. Geophys. Res. Atmos., **125**, e2019JD031172, https://doi.org/10.1029/2019JD031172.

Nag, A., and K. L. Cummins, 2017: Negative first stroke leader characteristics in cloud-to-ground lightning over land and ocean. *Geophys. Res. Lett.*, **44**, 1973–1980, https://doi.org/10.1002/2016GL072270.

NASA, 2018: GOES-R Series Data Book. NASA publication NP-2018-1-155-GSFC, 240 pp., https://www.goes-r.gov/downloads/resources/documents/GOES-RSeriesDataBook.pdf.

Nesbitt, S. W., D. J. Gochis, and T. J. Lang, 2008: The diurnal cycle of clouds and precipitation along the Sierra Madre Occidental observed during NAME-2004: Implications for warm season precipitation estimation in complex terrain. *J. Hydrometeor.*, **9**, 728–743, https://doi.org/10.1175/2008JHM939.1.

Ortéga, P., and T. Guignes, 2007: Lightning activity analyses with respect to the SPCZ location. *Geophys. Res. Lett.*, **34**, L11807, https://doi.org/10.1029/2007GL029730.

Orville, R. E., and G. R. Huffines, 2001: Cloud-to-ground lightning in the United States: NLDN results in the first decade, 1989–98. *Mon. Wea. Rev.*, **129**, 1179–1193, https://doi.org/10.1175/1520-0493(2001)129<1179:CTGLIT>2.0.CO;2.

Pavolonis, M. J., J. M. Sieglaff, and J. L. Cintineo, 2020: Remote sensing of volcanic ash with the GOES-R Series. *The GOES-R Series*, S. Goodman et al., Eds., Elsevier, 103–124.

Pessi, A. T., and S. Businger, 2009: Relationships among lightning, precipitation, and hydrometeor characteristics over the North Pacific Ocean. *J. Appl. Meteor. Climatol.*, **48**, 833–848, https://doi.org/10.1175/2008JAMC1817.1.

Peterson, M., 2019: Research applications for the Geostationary Lightning Mapper operational lightning flash data product. *J. Geophys. Res. Atmos.*, **124**, 10 205–10 231, https://doi.org/10.1029/2019JD031054.

——, 2021: Where are the most extraordinary lightning megaflashes in the Americas? *Bull. Amer. Meteor. Soc.*, https://doi.org/10.1175/BAMS-D-20-0178.1, in press.

——, W. Deierling, C. Liu, D. Mach, and C. Kalb, 2017: The properties of optical lightning flashes and the clouds they illuminate. *J. Geophys. Res. Atmos.*, **122**, 423–442, https://doi.org/10.1002/2016JD025312.

——, S. Rudlosky, and D. Zhang, 2020: Changes to the appearance of optical lightning flashes observed from space according to thunderstorm organization and structure. *J. Geophys. Res. Atmos.*, **125**, e2019JD031087, https://doi.org/10.1029/2019JD031087.

Rasmussen, K. L., M. D. Zuluaga, and R. A. Houze, 2014: Severe convection and lightning in subtropical South America. *Geophys. Res. Lett.*, **41**, 7359–7366, https://doi.org/10.1002/2014GL061767.

Rodger, C. J., J. B. Brundell, R. L. Dowden, and N. R. Thomson, 2004: Location accuracy of long distance VLF lightning location network. *Ann. Geophys.*, **22**, 747–758, https://doi.org/10.5194/angeo-22-747-2004.

Rudlosky, S., S. Goodman, K. Calhoun, C. Schultz, A. Back, B. Kuligowski, S. Stevenson, and C. Gravelle, 2020: Geostationary Lightning Mapper value assessment. NOAA Tech. Rep. NESDIS 153, 46 pp., https://doi.org/10.25923/2616-3v73.

——, ——, K. S. Virts, and E. C. Bruning, 2019: Initial Geostationary Lightning Mapper observations. *Geophys. Res. Lett.*, **46**, 1097–1104, https://doi.org/10.1029/2018GL081052.

Rutledge, S. A., K. A. Hilburn, A. Clayton, B. Fuchs, and S. D. Miller, 2020: Evaluating Geostationary Lightning Mapper flash rates within intense convective storms. *J. Geophys. Res. Atmos.*, **125**, e2020JD032827, https://doi.org/10.1029/2020JD032827.

Said, R. K., M. B. Cohen, and U. S. Inan, 2013: Highly intense lightning over the oceans: Estimated peak currents from global GLD360 observations. *J. Geophys. Res. Atmos.*, **118**, 6905–6915, https://doi.org/10.1002/jgrd.50508.

Schultz, C. J., V. P. Andrews, K. D. Genareau, and A. R. Naeger, 2020: Observations of lightning in relation to transitions in volcanic activity during the 3 June 2018 Fuego Eruption. *Sci. Rep.*, **10**, 18015, https://doi.org/10.1038/s41598-020-74576-x.

Sullivan, P. C., 2020: GOES-R series spacecraft and instruments. The GOES-R Series, S. Goodman et al., Eds., Elsevier, 13–21.

Thornton, J. A., K. S. Virts, R. H. Holzworth, and T. P. Mitchell, 2017: Lightning enhancement over major oceanic shipping lanes. *Geophys. Res. Lett.*, **44**, 9102–9111, https://doi.org/10.1002/2017GL074982.

Virts, K. S., J. M. Wallace, M. L. Hutchins, and R. H. Holzworth, 2013: Highlights of a new ground-based, hourly global lightning climatology. *Bull. Amer. Meteor. Soc.*, **94**, 1381–1391, https://doi.org/10.1175/BAMS-D-12-00082.1.

——, ——, ——, and ——, 2015: Diurnal and seasonal lightning variability over the Gulf Stream and the Gulf of Mexico. *J. Atmos. Sci.*, **72**, 2657–2665, https://doi.org/10.1175/JAS-D-14-0233.1.

Waliser, D. E., and X. Jiang, 2015: Tropical meteorology: Intertropical convergence zone. *Encyclopedia of Atmospheric Sciences*, 2nd ed. G. R. North, J. Pyle, and F. Zhang, Eds., Elsevier, 121–131.

Wang, F., H. Liu, W. Dong, Y. Zhang, and Q. Meng, 2018: Characteristics of lightning flashes associated with the charge layer near the 0°C isotherm in the stratiform region of mesoscale convective systems. *J. Geophys. Res. Atmos.*, **123**, 9524–9541, https://doi.org/10.1029/2018JD028569.

Weiss, S. A., D. R. MacGorman, and K. M. Calhoun, 2012: Lightning in the anvils of supercell thunderstorms. *Mon. Wea. Rev.*, **140**, 2064–2079, https://doi.org/10.1175/MWR-D-11-00312.1.

Williams, E., and Coauthors, 2002: Contrasting convective regimes over the Amazon: Implications for cloud electrification. *J. Geophys. Res.*, **107**, 8082, https://doi.org/10.1029/2001JD000380.

——, T. Chan, and D. Boccippio, 2004: Islands as miniature continents: Another look at the land-ocean lightning contrast. *J. Geophys. Res.*, **109**, D16206, https://doi.org/10.1029/2003JD003833.

Wodzicki, K. R., and A. D. Rapp, 2016: Long-term characterization of the Pacific ITCZ using TRMM, GPCP, and ERA-Interim. *J. Geophys. Res. Atmos.*, **121**, 3153–3170, https://doi.org/10.1002/2015JD024458.

Zhang, D., and K. L. Cummins, 2020: Time evolution of satellite-based optical properties in lightning flashes, and its impact on GLM flash detection. *J. Geophys. Res. Atmos.*, **125**, e2019JD032024, https://doi.org/10.1029/2019JD032024.